NON-STATIONARY ITERATIVE TIME-DOMAIN DECONVOLUTION FOR ENHANCING THE RESOLUTION OF SHALLOW SEISMIC DATA

by

Erhan Ergun

A Thesis

Submitted to the Faculty of Purdue University

In Partial Fulfillment of the Requirements for the degree of

Master of Science

Department of Earth, Atmospheric, & Planetary Sciences

West Lafayette, Indiana

August 2019

THE PURDUE UNIVERSITY GRADUATE SCHOOL
STATEMENT OF COMMITTEE APPROVAL

Dr. Robert L. Nowack

Department of Earth, Atmospheric and Planetary Sciences

Dr. Lawrence W. Braile

Department of Earth, Atmospheric and Planetary Sciences

Dr. Doug Schmitt, Chair

Department of Earth, Atmospheric and Planetary Sciences

Approved by:

Dr. Daniel J. Cziczo

Head of the Graduate Program

To my family

ACKNOWLEDGMENTS

I would like to thank my advisor Prof. Robert L. Nowack for his guidance, support and encouragement throughout my graduate studies. I am also grateful to my committee members, Prof. Doug Schmitt and Prof. Larry W. Braile, for serving on my committee. I also thank General Directorate of State Hydraulic Works (DSI), Turkey for supporting my graduate studies at Purdue University.

I also express my very deep gratitude to my parents and to my friends for providing me with continuous support and encouragement throughout my life and graduate school studies. Thank you for everything you have wished and done for me.

TABLE OF CONTENTS

LIST OF TABLES

LIST OF FIGURES

Figure Page

Figure Page

Figure Page

Figure Page

ABSTRACT

Author: Ergun, Erhan. MS
Institution: Purdue University
Degree Received: August 2019
Title: Non-stationary Iterative Time-Domain Deconvolution for Enhancing the Resolution of Shallow Seismic Data
Committee Chair: Doug Schmitt

The resolution of near-surface seismic reflection data is often limited by attenuation and scattering in the shallow subsurface which reduces the high frequencies in the data. Compensating for attenuation and scattering, as well as removing the propagating source wavelet in a time-variant manner can be used to improve the resolution. Here we investigate continuous non-stationary iterative time-domain deconvolution (CNS-ITD), where the seismic wavelet is allowed to vary along the seismic trace. The propagating seismic wavelet is then a combination of the source wavelet and the effects of attenuation and scattering effects, and can be estimated in a data-driven manner by performing a Gabor decomposition of the data. For each Gabor window, the autocorrelation is estimated and windowed about zero lag to estimate the propagating wavelet. Using the matrix-vector equations, the estimated propagating wavelets are assigned to the related columns of a seismic wavelet matrix, and these are then interpolated to the time location where the maximum of the envelope of the trace occurs within the iterative time-domain deconvolution. Advantages of using this data-driven, time-varying approach include not requiring prior knowledge of the attenuation and scattering structure and allowing for the sparse estimation of the reflectivity within the iterative deconvolution. We first apply CNS-ITD to synthetic data with a time-varying attenuation, where the method successfully identified the reflectors and increased the resolution of the data. We then applied CNS-ITD to two observed shallow seismic reflection datasets where improved resolution was obtained.

CHAPTER 1. INTRODUCTION

In many engineering and environmental problems, it is necessary to obtain detailed information about the near-surface geology. The shallow seismic reflection method has the potential of providing more detailed imaging compared to other seismic methods, such as refraction and surface wave methods. The primary target depths in shallow seismic exploration is in the tens to hundreds of meters depth range. Compared to seismic reflection imaging for greater target depths, shallow seismic reflection surveys image near surface layers that often have high seismic attenuation. This can limit the higher frequency components that are associated with higher resolution of shallow seismic data. Intrinsic attenuation can be expressed using the following equation

$$A_x = A_0 e^{-ax}, \tag{1.1}$$

where A_0 is the initial amplitude of the wave, A_x is the amplitude of the same wave at a distance x. The attenuation factor a can be expressed in terms of the quality factor, Q, and wavelength, λ, as

$$a = \frac{\pi}{Q\lambda} \tag{1.2}$$

Typical intrinsic attenuation Q values of some near surface materials are shown in Table 1-1. Here, smaller Q values signify a greater attenuation. Higher attenuation in the near-surface often occurs in unconsolidated clay and sand materials (Steeples, 2005). Note that attenuation also involves other effects in addition to intrinsic attenuation including scattering and diffraction effects.

Seismic deconvolution and inverse Q filtering can be used to improve the resolution of seismic data. Seismic deconvolution is a technique used to remove the effects of the seismic wavelet and can increase the frequency bandwidth of the deconvolved seismic data (Robinson, 1967; Yilmaz, 2001). Seismic deconvolution is often based on the assumption that the seismic trace is described by a time-invariant convolutional model, meaning the seismic wavelet does not change with propagation. In practice, however, seismic data are often non-stationary due to changes in the character and frequency content of seismic waves as they propagate through the subsurface. Seismic waves will lose amplitude and broaden with time because of losing high frequencies from intrinsic attenuation and scattering effects, and are therefore often more appropriately described as a combination of time-invariant and time-variant processes.

There are several time-variant deconvolution approaches to estimate the reflectivity. To obtain the propagating wavelets at different times, the seismic trace can be divided into several overlapping windows and the propagating wavelets estimated in these windows can then be used to recover the local reflectivity and compensate for the attenuation and scattering effects. The windowed segments of the seismic trace can then be blended together to obtain the full reflectivity.

Gabor deconvolution (Margrave and Lamoureux, 2001; 2019, Margrave et al., 2005) and time-variant spectral whitening (Yilmaz, 2001) have been proposed to deal with these non-stationary effects. Inverse Q filtering can be used to compensate specifically for the effects of seismic attenuation (Kjartansson, 1979; Hale, 1981) and is sometimes applied within a broader seismic imaging context (Wang, 2002; 2006; 2008). Lari and Gholami (2019) investigated multichannel non-stationary blind deconvolution using a non-stationary block overlap convolutional model and a variational approach. Morozov et al., (2018) presented an approach for time-varying deconvolution using iterative time-domain deconvolution. Their approach is based

on forward modeling of the seismic wavelet that can be estimated from the early arrivals of the seismic trace using the knowledge of a Q model and iteratively removing the modeled seismic wavelet from the seismic trace assuming that the propagating wavelet is not changing within short time windows. The disadvantage of inverse Q filtering method is that it requires the knowledge of a Q model. If the suitable Q values are provided, for instance from well logs, inverse Q filtering can successfully remove the attenuation effect from the seismic traces, but not other time-varying effects.

Using Gabor deconvolution based on the non-stationary convolutional model of Margrave (1998), deconvolution and inverse Q filtering can be combined without requiring explicit knowledge of Q in a fully data-driven frequency-domain approach. Similar to other frequency-domain deconvolution approaches, Gabor deconvolution can amplify the high-frequency noise in the seismic data. It also assumes a stationary propagating seismic wavelet over the individual windowed segments, which is not the case for a continuously changing propagating wavelet.

Here we investigate increasing the resolution of shallow seismic reflection data within the framework of a continuous non-stationary iterative time-domain deconvolution (CNS-ITD), where the propagating seismic wavelet is allowed to change continuously along the seismic data. CNS-ITD is performed iteratively in the time-domain which allows for the estimation of the largest reflectivities first, controls when to stop adding smaller reflectivity peaks, and has less sensitivity to noise compared to frequency-domain methods.

Table 1-1. Typical attenuation Q values of some near surface materials (from Steeples, 2005).

MATERIAL	Q-VALUES
Clay and sand	05–25
Sandstone	10–50
Shale	25–75
Granite	55–130
Limestone	50–180

CHAPTER 2. INITIAL OVERVIEW

Seismic data are often described by a convolution of the Earth's reflectivity with a seismic wavelet, and can be written as

$$y(t) = s(t) * r(t) = \int_{-\infty}^{\infty} s(t-\tau) r(\tau) d\tau \ , \tag{2.2}$$

where $*$ is the convolution operator, $y(t)$ is the seismic trace, $s(t)$ is the seismic wavelet, and $r(t)$ is the reflectivity. In seismic reflection imaging, seismic deconvolution is used to remove the effects of the seismic wavelet and to estimate the reflectivity corresponding to a layered Earth. Performing seismic deconvolution, however, often has two unknown functions, the seismic wavelet and the reflectivity series, and only one known function, the observed seismic trace. This is sometimes referred to as blind deconvolution, which is deconvolution without the explicit knowledge of either the seismic wavelet or the reflectivity. This can be solved, but requires additional assumptions. Robinson (1967) obtained the solution for blind deconvolution by assuming that the reflectivity is statistically white resulting in a flat power spectrum, and the seismic wavelet is minimum phase (Webster, 1978; Yilmaz, 2001). If the reflectivity is statistically white, any variability of the power spectrum of the seismic trace can be attributed to the seismic wavelet. Based on this, the power spectrum of the seismic wavelet can be estimated from the seismic data. Another assumption is that the casual seismic wavelet has minimum phase, and this enables the calculation of the seismic wavelet's phase spectrum from the power spectrum. For instance, Robinson (1966) states that dynamite sources used on land based seismic surveys produce minimum phase wavelet. The source signature of the air-gun used on marine seismic

surveys is also close to minimum phase (Hargeaves, 1992). When this is not the case, other techniques can be applied (Webster, 1978; Robinson and Osman, 1996).

In conventional seismic processing, the seismic wavelet is assumed to be invariant along the seismic trace, and the amplitude and shape of the seismic wavelet do not change as it propagates in the subsurface. In practice, however, the seismic wavelet can change due to seismic attenuation and scattering effects in the Earth. Thus, the conventional convolutional model is often insufficient in representing non-stationary effects on the seismic data. The stationary convolution model can, however, be extended to the non-stationary case using more general matrix-vector operations (Margrave, 1998; Margrave and Lamoureux, 2019).

Equation (2.1) can be implemented numerically as a matrix multiplication by assigning the seismic trace $y(t)$ and the reflectivity $r(t)$ as column vectors, $\boldsymbol{y}$ and $\boldsymbol{r}$ respectively, and by constructing an $\boldsymbol{S}$ matrix which includes the seismic wavelet as

$$\boldsymbol{y} = \boldsymbol{S}\boldsymbol{r}. \tag{2.2}$$

For the stationary case, $\boldsymbol{S}$ is a Toeplitz matrix formed by progressively time-shifted version of the same seismic wavelet $s(t)$ along the columns of $\boldsymbol{S}$. The matrix multiplication in Equation (2.2) involves multiplying each sample of the reflectivity series by the columns of the $\boldsymbol{S}$ matrix. Superpositions of the scaled and delayed seismic wavelets are then produced, and this represents the convolution process. Figure 2-1 illustrates the numerical implementation of stationary convolution using matrix-vector operations.

When the seismic wavelet changes in time, for example when attenuation is present, the matrix-vector multiplication above can still be applied, however, in this case, the $\boldsymbol{S}$ matrix no longer has Toeplitz symmetry (Margrave, 1998; Margrave and Lamoureux, 2019). The non-stationary character of the seismic trace may be caused not only by attenuation but also by other

effects, such as seismic scattering, that can alter the propagating seismic wavelet resulting in an amplitude reduction and a loss of frequencies.

Equation (2.1) can be extended to the non-stationary convolutional model by embedding a non-stationary function $a(t,\tau)$ as

$$y(t) = s'(t) * \int_{-\infty}^{\infty} a(t-\tau,\tau)r(\tau)d\tau = s'(t) * a(t,\tau) \odot r(t) \ , \tag{2.3}$$

where $*$ and $\odot$ represent the stationary and non-stationary convolution operators, respectively, and $y(t)$ now denotes the non-stationary seismic trace. For example, in the frequency domain, the non-stationary operator can be written as

$$a(t,\tau) = \int_{-\infty}^{\infty} A(t,f)e^{i\phi(t,f)}e^{i2\pi f\tau}df \ , \tag{2.4}$$

where $A(t,f)$ and $\phi(t,f)$ are the amplitude spectrum and phase spectrum of $a(t,\tau)$. For a constant Q seismic attenuation model of Kjartasson (1979) $A(t,f)$ can be written as

$$A(t,f) = e^{\frac{\pi|f|t}{Q}} \ . \tag{2.5}$$

For this model, the phase spectrum $\phi(t,f)$ can be obtained from the Hilbert transform over frequency of the natural logarithm of $A(t,f)$. The matrix equivalent of equation (2.3) can then be written as

$$\boldsymbol{y} = \boldsymbol{S'Ar} \ . \tag{2.6}$$

If we set $\boldsymbol{S} = \boldsymbol{S'A}$, the non-stationary matrix operation, similar to the stationary case, can be combined as

$$\boldsymbol{y} = \boldsymbol{Sr} \ . \tag{2.7}$$

where $\boldsymbol{S}$ is now a non-Toeplitz matrix containing the attenuated propagating seismic wavelet, $\boldsymbol{r}$ is a vector for the reflectivity series, and $\boldsymbol{y}$ is the output seismic trace. Figure 2.2 depicts the non-

stationary convolutional model. The matrix $\boldsymbol{S}$ in this figure represents the propagating seismic wavelet changing in time according to the attenuation operator given in equation (2.4).

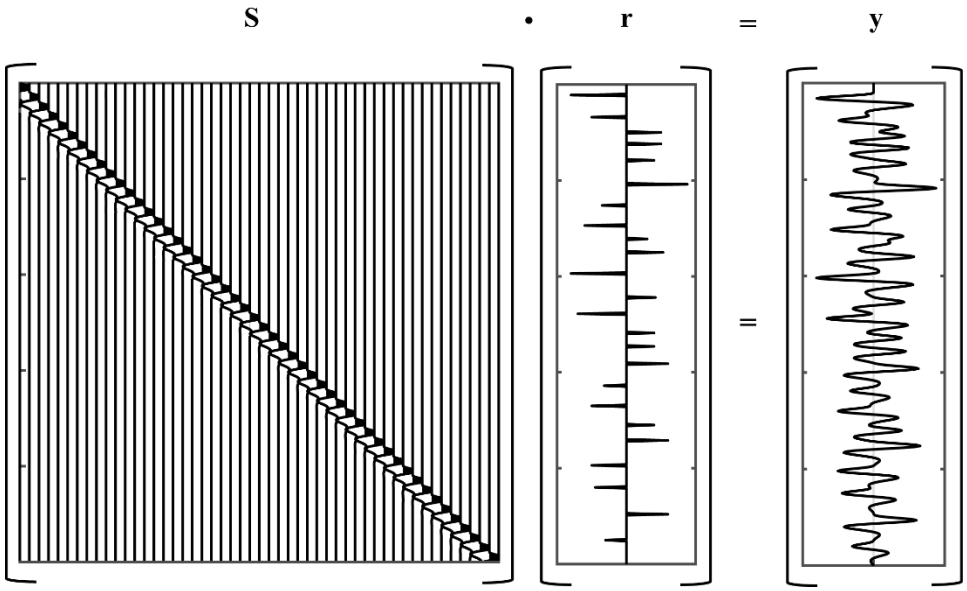

Figure 2-1. This illustrates stationary convolution where a Toeplitz S matrix with the columns containing shifted seismic wavelets is multiplied by the r vector representing the reflectivity and y is the output seismic trace.

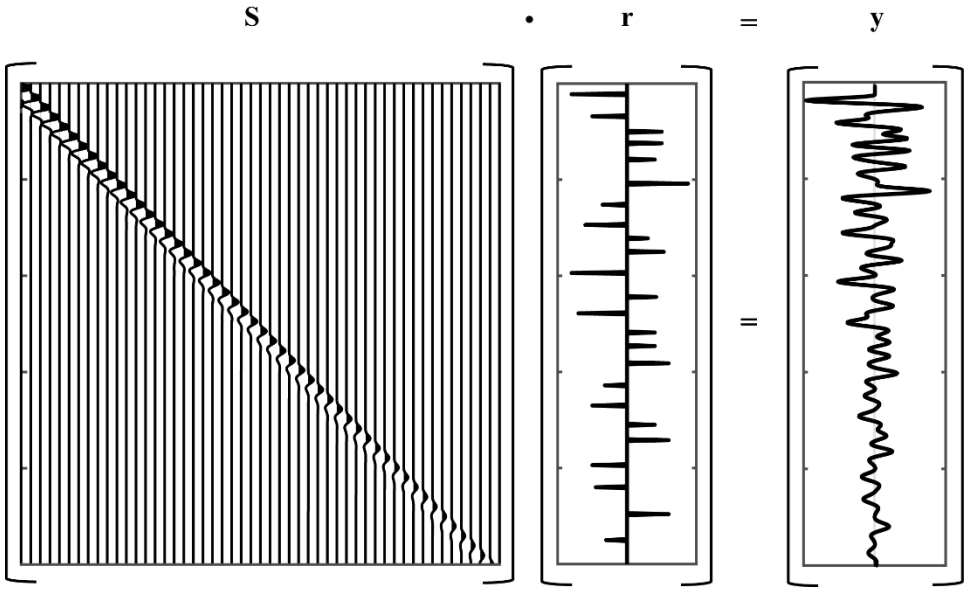

Figure 2-2. This illustrates non-stationary convolution where a non-Toeplitz S matrix contains the delayed propagating seismic wavelets which are now changing in time. The vector r represents the reflectivity and y the output seismic trace. In this example, the seismic wavelet is attenuated with an attenuation operator with Q=50.

CHAPTER 3. METHOD

Iterative time-domain deconvolution (ITD) was described by Kikuchi and Kanamori (1982), and Ligorría and Ammon (1999) applied this to the estimation of seismic receiver functions. The ITD approach can also be used to iteratively reconstruct the reflectivity in shallow seismic reflection surveys. To implement this, the seismic wavelet and the seismic trace are first cross-correlated, and the maximum is found to locate the strongest reflectivity. This estimate of the reflectivity is then convolved with the seismic wavelet to obtain a predicted output trace, and the result is subtracted from the seismic trace to form a residual trace. This process is iterated until the mean square error (MSE) between the observed and predicted trace has sufficiently decreased. This is illustrated in Figure 3-1 which shows a synthetic seismic trace formed by the convolution of a seismic wavelet with a reflectivity series including 4 reflectors. One percent Gaussian noise has also been added to the seismic trace. The estimated reflectivity at the final iteration is shown in Figure 3-1 and is a good match with the true reflectivity. As is seen, knowledge of the seismic wavelet is required but this can be estimated from seismic trace.

The ITD approach can be viewed as searching for a seismic wavelet across the seismic trace. Whenever there is a match, the algorithm removes the seismic wavelet and puts a spike at that location. Like other deconvolution methods, the ITD method is typically designed for stationary signals. However, by modifying the algorithm, it can also be applied to remove non-stationary propagating seismic wavelets (Morozov et al., 2018). The reflectivity series can then be iteratively updated from non-stationary template matching. The ITD approach has several desirable characteristics which include finding the largest reflectivities first, providing control over when to stop adding smaller peaks, and also can have less sensitivity to noise compared to frequency-domain deconvolution methods.

Using the Equation (2.2) the reflectivity series can be iteratively found as

$$\boldsymbol{y}^{i+1} = \boldsymbol{y}^{i} - r_i * (\boldsymbol{S}_{column\ j}) \,, \tag{3.1}$$

where * denotes convolution, i is the iteration number, $\boldsymbol{S}_{column\ j}$ is the j^{th} column of the $\boldsymbol{S}$ matrix, and the reflection coefficient r_i is then found by

$$r_i = \frac{(\boldsymbol{S}_{column\ j})^{\boldsymbol{T}}\ \boldsymbol{y}^{i}}{(\boldsymbol{S}_{column\ j})^{\boldsymbol{T}}(\boldsymbol{S}_{column\ j})}. \quad i = 1,2,3 \dots \dots N \tag{3.2}$$

The largest peaks in the dot product $(\boldsymbol{S}_{column\ j})^{T}\boldsymbol{y}^{i}$ can be used to determine the sequential values for the reflection coefficient r_i at the i^{th} iteration. The location of the peak value of this multiplication gives the arrival time for that event and the result is then normalized by the dot product of the j^{th} column of $\boldsymbol{S}$ with itself to obtain an estimate of the reflection coefficient r_i at the i^{th} iteration. After finding the first reflectivity coefficient and its location, we convolve it with the j^{th} column of the $\boldsymbol{S}$, and subtract this from the seismic trace to find $\boldsymbol{y}^{i+1}$ for the next iteration.

The construction of the $\boldsymbol{S}$ matrix, and therefore knowledge of the seismic wavelet is required to implement the algorithm given above. However, once the seismic wavelets have been estimated, specific columns of $\boldsymbol{S}$ can be obtained for each iteration. There are a number of ways of estimating the seismic wavelet. Here we use an approach to determine the propagating seismic wavelet which assumes that the reflectivity is statistically white resulting in a flat power spectrum. The autocorrelation of the reflectivity is then approximately a delta function at zero lag. The autocorrelation of the source wavelet convolved with the reflectivity then approximately equals the autocorrelation of the source wavelet, and this will be equal to the autocorrelation of the seismic trace. However, in practice, the autocorrelation of the reflectivity is not exactly zero at other lags, thus a windowed autocorrelation can be used to estimate the seismic wavelet. In the frequency-domain, this results in

$$|S(f)|^2 \cong |Y_s(f)|\,, \tag{3.3}$$

where $|Y_s(f)|^2$ is the smoothed power spectrum of the seismic trace, or the Fourier transform of the tapered auto-correlation, and $|S(f)|^2$ is the power spectrum of the seismic wavelet. The power spectrum of the seismic wavelet can then be estimated from the tapered autocorrelation of the seismic trace.

Figure 3-2 illustrates the wavelet estimation process for the stationary case. First, using the reflectivity series shown in Figure 3-2a, a synthetic trace is formed by convolving the reflectivity series with a seismic wavelet in Figure 3-2b. The autocorrelation of the seismic trace is found, and this is then windowed around zero lag as in Figure 3-2c. Here, a shorter window length produces a smoother power spectrum, however, this may lack the full characteristics of the seismic wavelet. On the other hand, a long window length produces a less smooth power spectrum resulting in a more oscillatory time-domain wavelet. Thus, an appropriate window length needs to be chosen. For an impulsive source, the second zero-crossing of the autocorrelogram can sometimes be used to produce a good estimation of seismic wavelet as in predictive deconvolution (Yilmaz, 2001). Figure 3-2d shows the resulting zero phase windowed autocorrelation. To obtain a casual wavelet, a minimum phase can be added to obtain a minimum phase seismic wavelet.

If the seismic wavelet is minimum phase, then its phase spectrum can be uniquely obtained from its amplitude spectrum. The minimum phase estimate is obtained by taking the Hilbert transform of the log amplitude spectrum (Robinson, 1967) which is given by

$$\Theta(f) = \boldsymbol{H}\{\ln|Y(f)| + \varepsilon\}. \tag{3.4}$$

Here $\boldsymbol{H}$ denotes the Hilbert transform, and to stabilize the Hilbert transform a small positive constant ε is added. After the phase information is incorporated, the minimum phase seismic wavelet can be obtained from its amplitude spectrum as

$$S(f) = |S(f)|e^{i\Theta(f)}. \tag{3.5}$$

Figure 3-2e shows the true minimum phase seismic wavelet for the synthetics (grey dashed) and estimated seismic wavelet (black).

In the case of a stationary seismic wavelet, the $\boldsymbol{S}$ matrix can be built using only one estimated seismic wavelet, and the auto- and cross-correlations can be performed using the fast Fourier transform, FFT. If the seismic wavelet is not stationary, non-stationary deconvolution requires different propagating seismic wavelets at different times to compensate for the changing characteristics of the wavelet along the seismic trace. One way to construct a non-stationary $\boldsymbol{S}$ matrix is to move a properly chosen time window across the seismic trace one time sample at a time, and estimating the propagating seismic wavelet in each time window. These can then be assigned to the related columns of $\boldsymbol{S}$. Although this provides a way for obtaining the changing seismic wavelet continuously, it is not a very efficient implementation, especially for long seismic traces. Instead, here we divide the trace into a smaller number of overlapping windows for the estimation of the propagating wavelet for the different time windows by using a partition of unity (POU) (Margrave and Lamoureux, 2001; Grossman et al., 2002; Margrave and Lamoureux, 2019).

A POU results in a set of windows that add to one as,

$$\sum_{k=1}^{M} \Omega(t - k\Delta t) = \sum_{k=1}^{M} \Omega_k = 1, \tag{3.6}$$

where M is the number of windows, and Ω_k is the window function shifted in time by $t = k\Delta t$ along the seismic trace. For example, a Gaussian window is given by

$$\Omega_k = \frac{\delta}{\lambda\sqrt{\pi}} \exp\left(-\frac{(t-k\delta)^2}{\lambda^2}\right), \tag{3.7}$$

where δ is the spacing between the windows, and λ is the Gaussian half-width. This window function can then be used to build the POU provided that $\delta \ll \lambda$. Wider and flatter windows with steeper slopes on the sides can also be used. (Margrave et al., 2011; Margrave and Lamoureux, 2019).

The main effect of the windowing is to decompose the seismic trace into smaller, localized sub-components by multiplying the signal with the window functions, where t_C is the center time of each window. This can be written as

$$y(t) = \sum_{k=1}^{M} y_k(t, t_c) = \sum_{k=1}^{M} \Omega_k(t, t_C) y(t) \ , \tag{3.8}$$

where $y_k(t, t_C)$ is the windowed segment of the seismic trace, and M is the number of windows. The windowed segments of the seismic trace can be thought of as resulting from the convolution of propagating seismic wavelets and local reflectivity in that window, and this can be represented as

$$y_k(t, t_c) \ \approx \ s(t, t_c) * r(t, t_c) \, , \tag{3.9}$$

where $s(t, t_c)$ is the locally stationary seismic wavelet in the window centered at t_c and $r(t, t_c)$ is the local reflectivity in that window. The seismic wavelet, $s(t, t_c)$, can then be estimated in each window and this carries information about the local propagating wavelet.

This approach assumes that the individual windowed segments of the seismic trace are locally stationary, and a stationary deconvolution can be applied within each window. For continuously varying propagating wavelets, locally stationary deconvolution would be less accurate unless the windows lengths are chosen to be small. However, the matrix-vector version

of the non-stationary convolution model can still be applied. To perform non-stationary deconvolution for a continuously varying seismic wavelet, the propagating seismic wavelets can be continuously interpolated in time so as to change smoothly along the seismic trace. Once the propagating wavelets are estimated in each window, these can then be assigned to corresponding columns of the $\boldsymbol{S}$ matrix at the center times of the windows. In this way, only several columns of the $\boldsymbol{S}$ matrix are initially estimated. Other columns of the $\boldsymbol{S}$ matrix can then be found as needed by interpolation within the iterative process from a smaller number of estimated propagating wavelets. Here, we estimate the corresponding columns of the $\boldsymbol{S}$ matrix from the peaks of the envelope of the seismic trace, instead of the peaks of the cross-correlation.

The distinction between the approach followed here and that of Margrave et al., (2011) and Margrave and Lamoureux, (2019) in the frequency-domain, and Morozov et al., (2018) using the iterative time-domain approach is that the propagating wavelet is allowed to vary continuously along the seismic trace. We refer to this as continuous non-stationary iterative time-domain deconvolution (CNS-ITD).

3.1 Synthetic Example

To illustrate the CNS-ITD process, a synthetic example is used to evaluate our approach in both the stationary and non-stationary cases. The seismic wavelets are estimated in sub-windows and used to construct selected columns of the S matrix. In the stationary case, the FFT can be used to obtain the cross- and auto-correlations for the ITD approach. Here we apply the CNS-ITD approach with a matrix-vector approach.

For the first example, the seismic wavelet is assumed to be stationary along the seismic trace, and all the columns of the S matrix can be filled with one estimate of the seismic wavelet

estimated from the entire seismic trace. Even though we can construct the full S matrix, it does not mean that in the iteration process, all the columns will be used for estimating the reflectivity series. At each iteration of the CNS-ITD process, only one column of the S matrix is used and this significantly reduces the computation time compared to full matrix-vector multiplications. We estimate the specific columns of the S matrix by the maximum peaks of the envelope of the seismic trace. In the case of a centered zero-phase wavelet, the location of the reflectivities and the peak of the envelope in the seismic trace are at the same location. For a casual seismic wavelet, however, there is a time shift between these two times. To address this, we use the difference between the beginning time and peak of the envelope of the estimated casual seismic wavelet as a time shift to correctly locate the reflectivity at the appropriate times as

$$\Delta t_i = t_i^e - t^0 , \tag{3.10}$$

where t^0 is the initial time and t_i^e is the time of the envelope peak of the estimated seismic wavelet. Once this time shift is found, the appropriate column of $\boldsymbol{S}$ can be determined. For the stationary case, the time shift Δt_i is a constant value along the entire seismic trace since the seismic wavelet is time-invariant. For the non-stationary case, where the propagating seismic wavelet is changing in time, the time shift also changes along the seismic trace. For a zeros phase wavelet, the time shift would be zero. Figure 3-3 compares the time shifts for two propagating seismic wavelets one early and one later in time along an attenuated seismic trace for a constant Q attenuation model.

Although a local stationary deconvolution could be applied for each windowed segment of the seismic trace, it is not ideal since it does not allow for a continuously varying seismic wavelet. For seismic attenuation, the seismic wavelet evolves continuously as it propagates even within windowed segments of the seismic trace, and this can be achieved by interpolation of the propagating seismic wavelets along the seismic trace.

Figure 3-4 illustrates the approach for the stationary case, where for each iteration, the maximum peaks of the envelope of the full seismic trace are sequentially found. The corresponding columns of the $\boldsymbol{S}$ matrix are chosen from the estimated seismic wavelet. Using the location of the maximum of the envelope of the seismic wavelet, Δt_i can be estimated and the columns of the $\boldsymbol{S}$ matrix found. Equation (3.2) is then applied to find the corresponding reflectivity shown on the right on Figure 3-4 for each iteration. The estimated reflectivities at each iteration are then adaptively removed from the seismic trace by applying Equation (3.1). Since this is an iterative process, we can terminate the process either by specifying the total number of iterations or by the reduction in the mean square error (MSE) between the predicted trace and the observed seismic trace. After the iteration process shown in Figure 3-4, all the reflectivities have been successfully recovered from the seismic trace, and MSE is close to the noise level added to the synthetic trace.

As noted previously, for the stationary case, the reflectivity can also be determined by calculating cross- and auto-correlations, which can be estimated using the FFT. For a comparison of the computation time, the same number of iterations have also been performed using the FFT to calculate the cross- and auto-correlations. The matrix-vector multiplications are slower compared to cross- and auto-correlations obtained by the FFT. The average computation time of the 24 iterations for a trace with 512 time samples using the FFT is 0.0019 s on a PC laptop using MATLAB. The time for the vector-vector operations, on the other hand, is 0.0061 s, which is several times slower than the FFT based operations. However, in the context of iterative time-domain deconvolution, we are only estimating the largest reflectivities which helps to reduce the costs of the matrix-vector operations.

Unlike stationary deconvolution, using one seismic wavelet for the non-stationary case produces incorrect results from not taking into account the non-stationary character of the seismic

trace. Figure 3-5 shows an example of what will happen if a non-stationary seismic trace is treated incorrectly as a stationary trace. As can be seen, especially at later times, the estimated reflectivity is underestimated and incorrectly located in time resulting from the changing character of the seismic trace.

To deal with the non-stationary case, the propagating seismic wavelets along the seismic trace are first estimated for windowed segments of the seismic trace. The length of the window is an important parameter that needs to be carefully determined. In practice, the window length should be at least longer than that of propagating seismic wavelet in order to get a good estimate of the propagating seismic wavelets. Also, the distance between the window centers should be small enough so that changes in the propagating wavelet can be estimated, particularly if the seismic attenuation varies rapidly. The propagating seismic wavelets are then estimated from the localized windowed segments of the seismic trace in a data-driven way, and not assuming a simple attenuation model. The propagating seismic wavelets can then be interpolated as required for the iterative estimation of the reflectivity.

Spectrograms are very useful in analyzing signals whose frequency content is changing in time. An example of the spectrogram of a synthetic non-stationary trace resulting from attenuation is shown in Figure 3-6. The amplitude spectrum is shown on the left for the non-stationary seismic trace shown at the bottom. It can be seen both from the seismic trace and spectrogram that the bandwidth of frequencies is being reduced by the non-stationary filtering. In particular, frequencies greater than 75 Hz are attenuated for later times, along with a loss of amplitude resulting, and this leads to a lower resolution of the seismic data for greater times.

Using window partitions of the seismic trace, estimates of the propagating seismic wavelets can then be made in each of the windows in order to construct selected columns of the $\boldsymbol{S}$ matrix.

Figure 3-7a) and b) depict the windows and estimated propagating wavelets at the center of each window. As can be seen, the propagating seismic wavelet is time-varying, losing amplitude and spectral content with time as shown in spectrogram in Figure 3-6. Using the center times of the windows, these are assigned to the columns of the S matrix which are shown in Figure 3-7c). These can then be interpolated to determine selected columns of the S matrix where the maximum values of the envelope of the seismic trace occur, including the time shift given in Equation 3.10. Continuous non-stationary iterative time-domain deconvolution (CNS-ITD) can then be performed to find the reflectivities along the seismic trace. As noted previously, an advantage of this approach is that it allows one to find any desired number of the strongest reflectivities, leading to a sparse deconvolution of the seismic trace.

Figure 3-8 illustrates the CNS-ITD of the seismic trace shown in a) where 1% Gaussian random noise has been added. We used a different number of iterations as shown in d) to estimate the full reflectivity series. For iteration, it=5, this gives five initial reflectivity estimates along the seismic trace. The residual traces in c) are then found by iteratively subtracting the predicted traces at each iteration. The residuals become smaller with an increasing number of iterations, and the mean square error (MSE) is reduced shown on the left. After 30 iterations, the full reflectivity series has been recovered. Note however that several smaller additional reflectivity values have also been found. Since the estimation of the propagating wavelets includes some errors in terms of waveform and amplitude, some residuals will be present between the predicted and true reflectivities resulting from this. If we further increase the iteration number, the ITD approach will treat the remaining residuals as signal and try to produce new reflectivities. However, since all the strongest reflectivities have been estimated and removed from the seismic trace, remaining reflectivities will be small. However, small artifact reflectivities can be avoided by limiting the

MSE error between the observed and predicted seismic trace. These can then be re-convolved with a stationary wavelet to construct high resolution seismic trace.

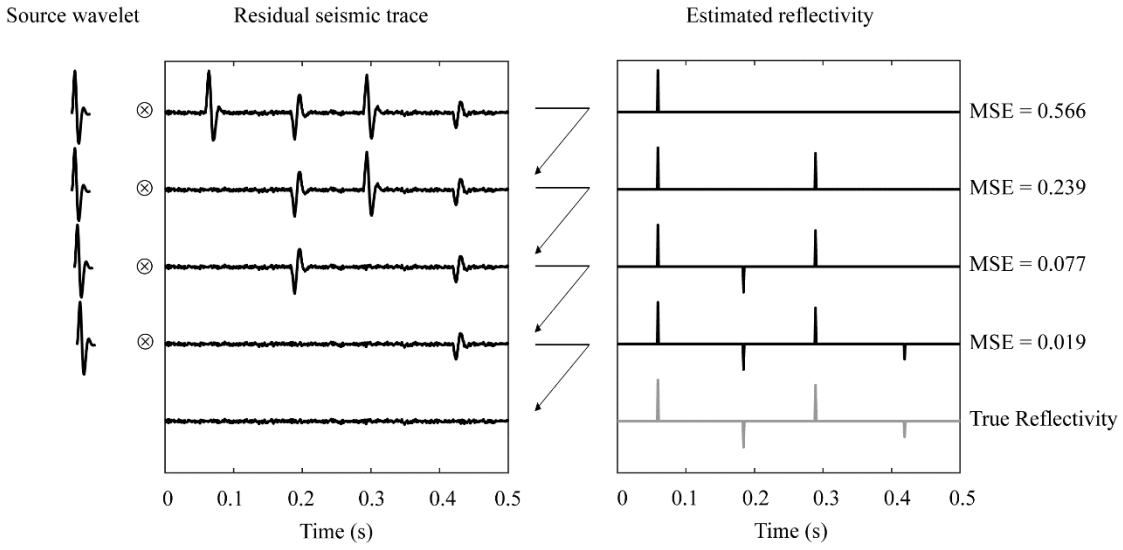

Figure 3-1. An illustration of iterative time-domain (ITD) deconvolution for the stationary case where 1% random noise has been added to the seismic trace. At each iteration, the reflectivity is determined by finding the maximum of the cross-correlation, denoted by ⊗, with the seismic wavelet shown on the left and the residual seismic trace is formed. To the right, the iteratively updated reflectivity is shown with the true reflectivity displayed at the bottom. The reduction of the mean square error (MSE) is shown on the far right for each iteration. The final output of the iterative time-domain deconvolution is seen to be a good match to the true reflectivity (gray).

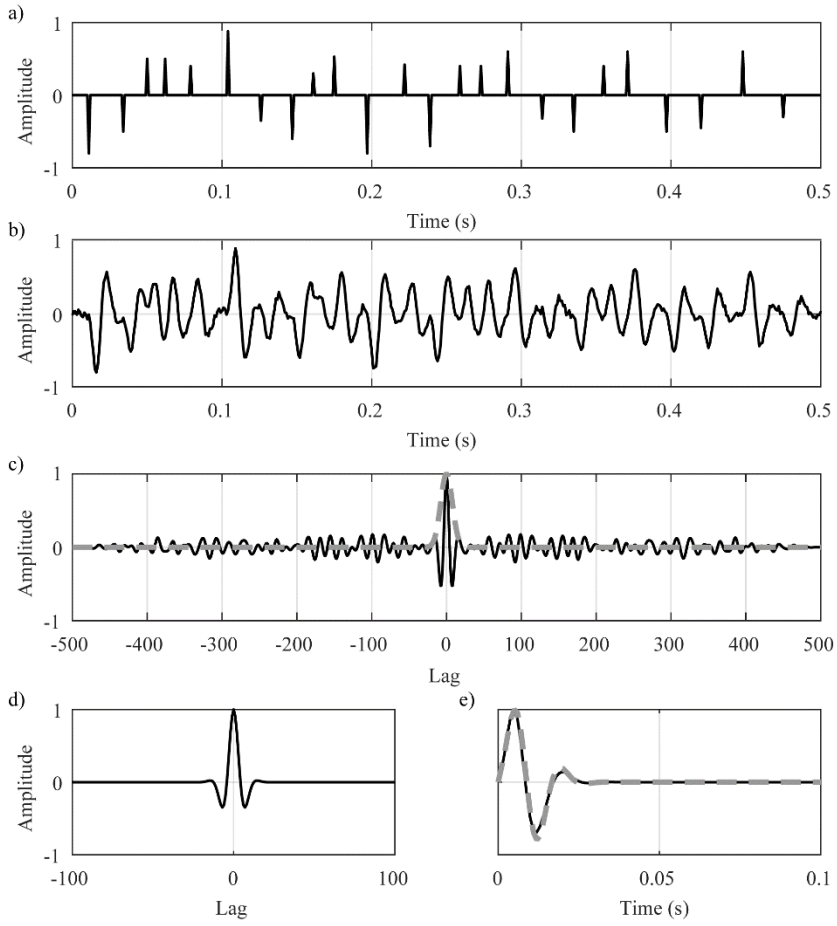

Figure 3-2. This illustrates the wavelet estimation process in the stationary case. a) shows the reflectivity series, and b) shows the seismic trace including where 1% Gaussian noise has also been added. c) shows the autocorrelation of the seismic trace. A Gaussian window is applied (dashed gray line) to the autocorrelation of the trace around the zero lag. d) shows the windowed autocorrelation of the seismic trace, and e) shows a minimum phase version of the estimated wavelet (black), and the true seismic wavelet (gray dashed) which for this example is also minimum phase.

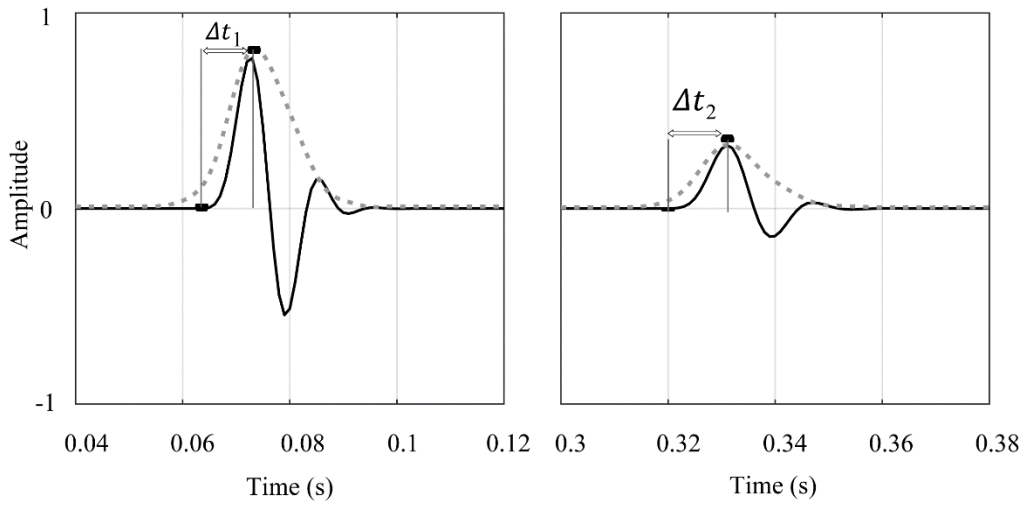

Figure 3-3. This shows the envelope time shifts Δt_1 and Δt_2 for two propagating seismic wavelets estimated at an early and late time along the seismic trace for a constant Q casual attenuation model. The black dots denote the locations of the initial time and peak of the envelopes (dashed-gray) of estimated seismic wavelets. The time for the maximum of the envelope peak is later for the second case since it has undergone a greater phase delay from the casual attenuation model.

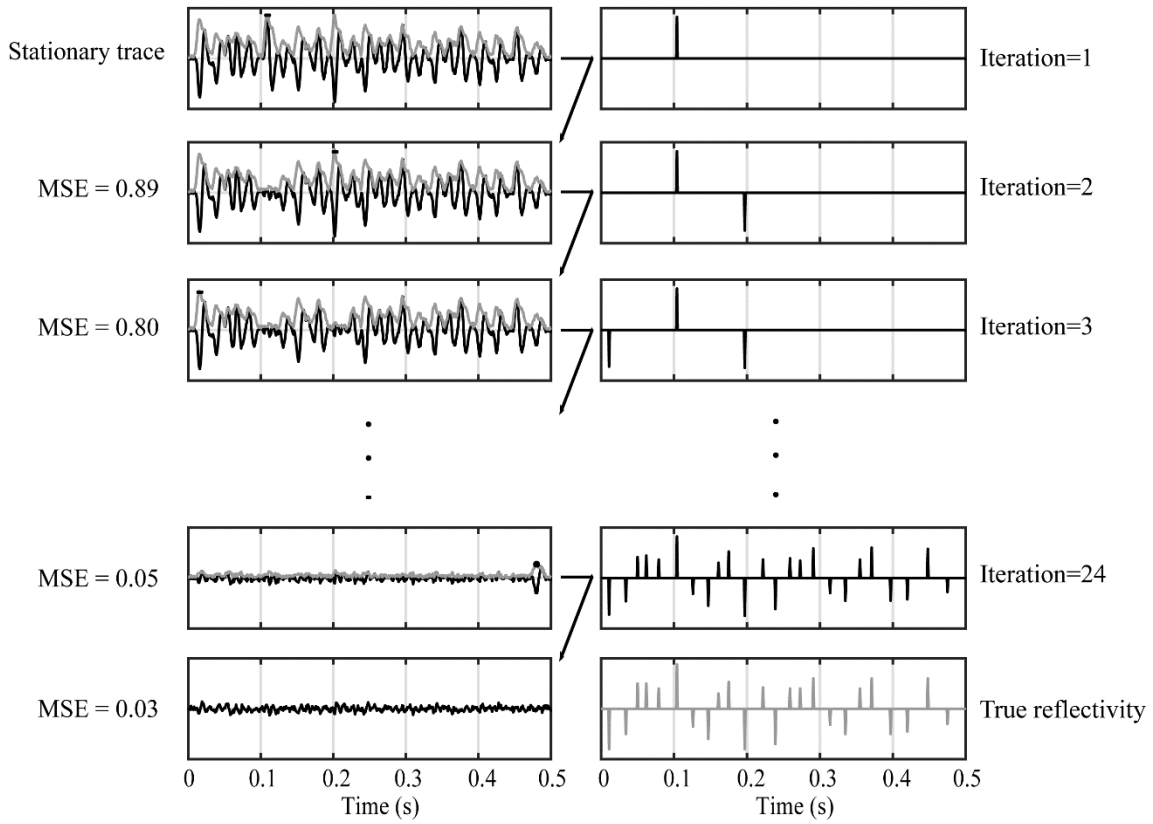

Figure 3-4. Iterative time domain deconvolution for the stationary case. The synthetic trace is shown on the top left and 1% Gaussian random noise has been added. At each iteration, the location of the maximum peak of the envelope of the seismic trace is found which is denoted by black dot, and the corresponding propagating wavelet is chosen from the column of the S accounting for the time shift Δt described in Equation (3.10). Using the seismic trace and the propagating wavelet, Equation (3.2) is applied to estimate the reflectivity shown on the right. The estimated reflectivity is then subtracted from the seismic trace for the next iteration. After a sufficient number of iterations, all the reflectivities are recovered from the seismic trace. The true reflectivity is shown on the bottom right.

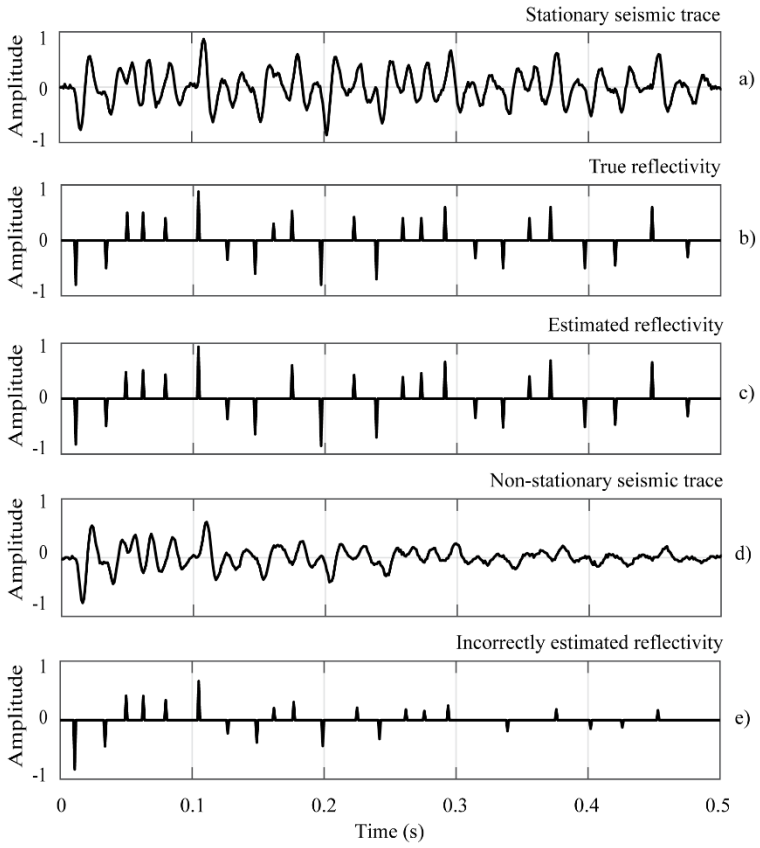

Figure 3-5. (a) shows a stationary seismic trace obtained using the true reflectivity (gray) in (b) and a stationary seismic wavelet. (c) shows the iterative time domain deconvolution for the stationary case, compared to the true reflectivity in (b). (d) shows the non-stationary seismic trace obtained for an attenuated seismic wavelet with an attenuation applied for a Q=50. (e) shows the incorrectly estimated reflectivity when a stationary deconvolution is applied to a non-stationary seismic trace.

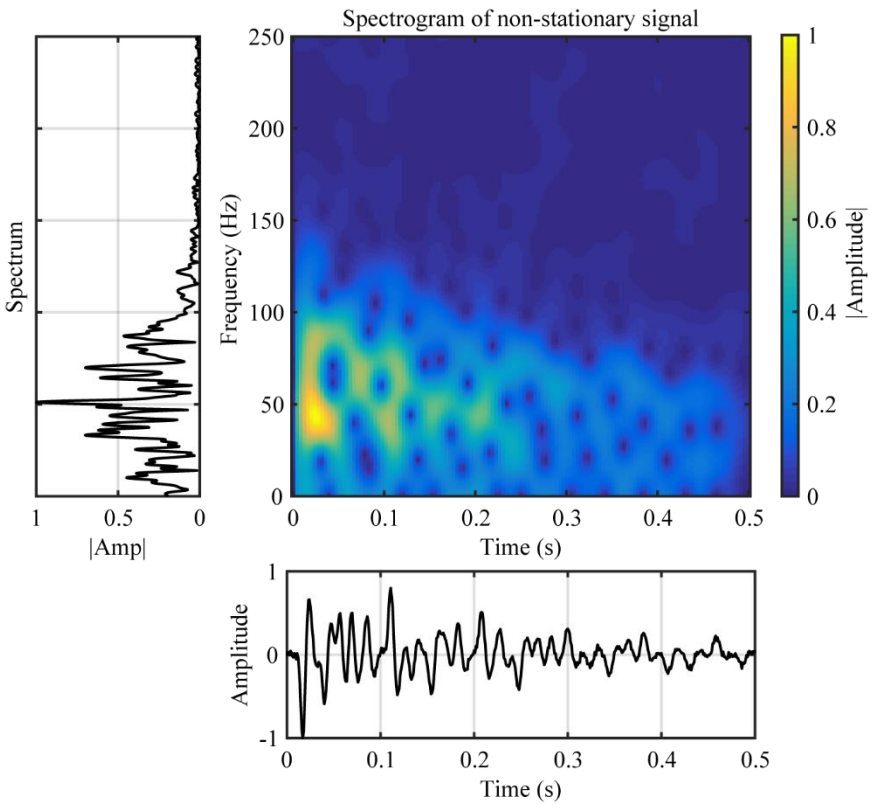

Figure 3-6. The spectrogram of a non-stationary seismic trace. The Fourier amplitude spectrum is shown on the left for the non-stationary seismic trace shown at the bottom. 1% Gaussian random noise has also been added to the non-stationary seismic trace. It can be seen that higher frequencies greater than 75 Hz are being reduced for increasing time for this example.

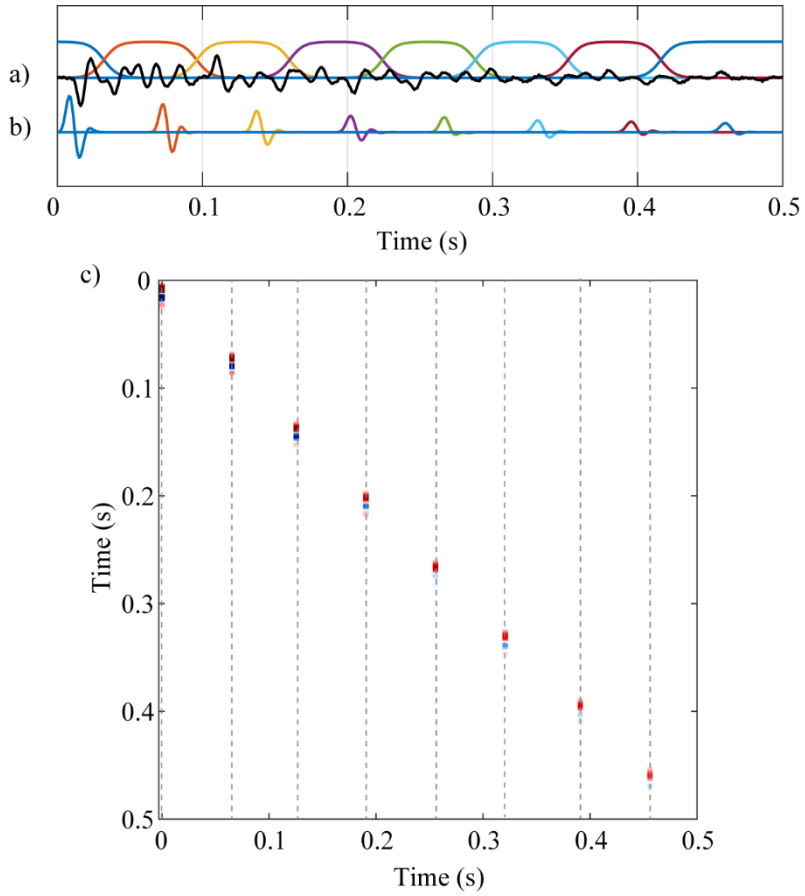

Figure 3-7. a) shows a non-stationary seismic trace along with windows functions used to window the seismic trace. b) shows the estimated propagating seismic wavelets for each of the window. c) shows the columns of the S matrix, where the propagating seismic wavelets are assigned to specific columns of S at the center times of the windows shown in light gray dashed lines. Once these columns of the S matrix have been found, other selected columns can be quickly estimated by interpolation, and used within the non-stationary ITD deconvolution.

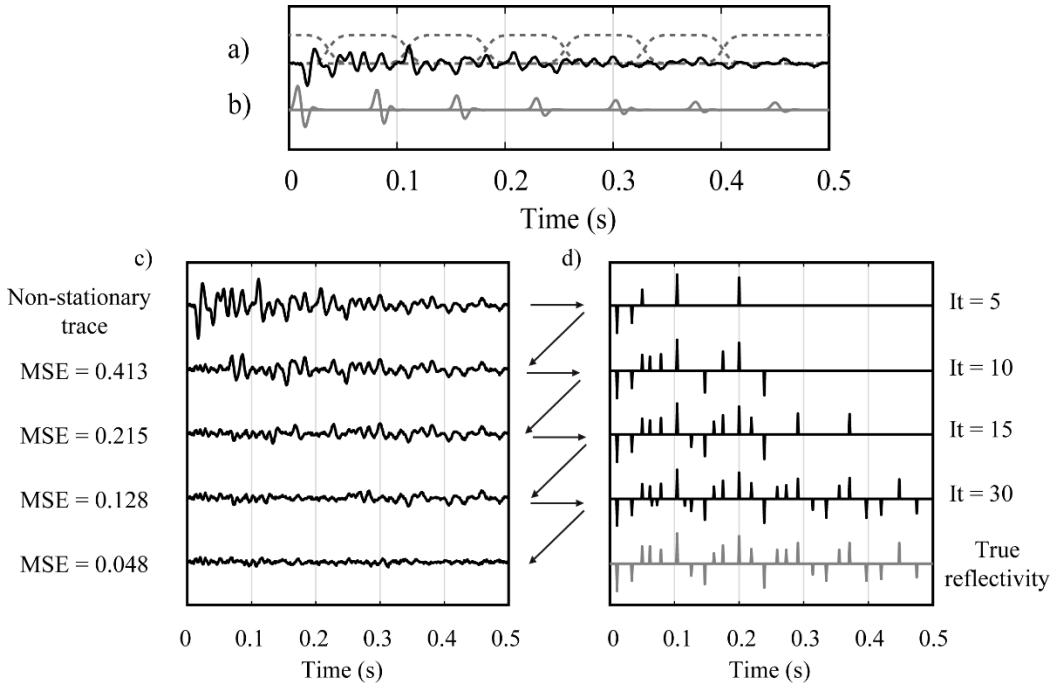

Figure 3-8. a) shows a non-stationary seismic trace and the window functions used. b) shows the estimated propagating wavelets in each window. c) shows the residual seismic traces where the top is the initial non-stationary trace and the residual traces below are after removing the estimated reflectivities at each iteration have been determined from the initial trace. Continuous non-stationary iterative time-domain deconvolution (CNS-ITD) is performed along the seismic trace showing in d) for different numbers of iterations. For It=5, five reflectivities are found along the seismic trace, and these are increased until all the reflectivities have been recovered. As the number of iterations is increased, the MSE error of the residual trace is decreased which can be seen in c). When the number of iterations is increased, the CNS-ITD approach will try to recover more reflectivities in d) from the residuals shown in c).

CHAPTER 4. OBSERVED DATA APPLICATIONS

We have applied the CNS-ITD approach to two observed shallow seismic reflection datasets from Baker (1999). The first dataset was collected in an alluvial valley of the Thames River, England in 1989 to image bedrock stratigraphy and examine the structure and geometry. Data acquisition parameters and equipment for Thames River dataset are given in Table 4-1. Figure 4-1a) shows the observed zero offset stacked data from Baker (1999). The horizontal axis in this figure is trace number and the spacing between the traces is 1.25 meters. The vertical axis is two-way reflection time down to 0.25 seconds. The processing steps applied to the data by Baker (1999) were pre-processing (geometry definition, killing the noisy traces), filtering the ground roll and air wave, static corrections, velocity analysis and stacking. To increase the lateral coherence, we have also applied some additional f-k filtering to enhance the continuity and coherence between traces (Figure 4-1b, Appendix A.). The non-stationary character of the seismic traces can be seen from the spectrogram for trace 10 shown in Figure 4-2 where the spectrogram amplitudes show a slight decrease in frequency with time. This frequency decrease in time is evident even with relatively small reflection travel-times due to the alluvial medium at the site that also can have higher attenuation (Steeples, 2005).

Before applying CNS-ITD to the seismic section, we perform it on a single trace in order to determine the window size and iteration number to be applied for each of the traces. Figure 4-3a) shows trace 10 used for the spectrogram in Figure 4-2 and the windows that were used for partitioning of the trace to estimate the propagating wavelet for different travel-times. Figure 4-3b) shows the estimated propagating wavelets for each of the windows. In this case, since the data have been previously processed by Baker (1999), we assume here that the non-stationary

propagating seismic wavelets are zero phase and normalized to unit amplitude. These are then continuously interpolated along the trace iteratively within the CNS-ITD process.

We have used both the mean square error (MSE) and the total number of iterations as stopping criteria in the iteration process. Thus, if the maximum iteration number is reached or the MSE between observed and predicted traces is below a specific level, the process is terminated. Figure 4-3c) shows trace 10 and residual traces calculated after application of CNS-ITD with different numbers of iterations given on the right side of the subplot, and it=10 signifies that ten iterations have been performed. The estimated spike diagrams for different numbers of iterations are shown in Figure 4-3d). After ten iterations, only the strongest reflectivities have been determined. When the number of iterations is increased, an increasing number of smaller reflectivities are obtained. When the iteration number has reached 60, the mean square error of the residual trace has been reduced to about 2 percent.

We then applied CNS-ITD to the entire shallow seismic section for the Thames River dataset. The output of the CNS-ITD are the deconvolved reflectivities similar to that shown in Figure 4-3d) for each trace, and are shown in Appendix B. Seismic sections can then be obtained using a stationary Ricker wavelet with different dominant frequencies, and these are shown in Appendix B. Figure 4-4a) shows the original stacked section from Figure 4-1b) and Figure 4-4b) shows the results of the CNS-ITD re-convolved with a stationary 250 Hz Ricker wavelet. An f-k filter was also applied slightly to increase the lateral coherency. To see the effect of the CNS-ITD on the seismic traces, we plot the spectrogram of the deconvolved trace 10 after CNS-ITD, and re-convolved with a stationary 250 Hz Ricker wavelet in Figure 4-5. Comparing the figures 4-2 and 4-5, it can be seen that the frequency bandwidth of the trace has been improved with more uniform and higher frequency content.

The second observed dataset was collected by Baker (1999) in Kansas to image if there was a glacial meltwater channel cut into the bedrock, and then later covered by sediments. Data acquisition parameters and equipment for Kansas dataset are given in Table 4-2. Similar processing steps applied to first dataset were also applied to the Kansas dataset by Baker (1999). Figure 4-6a) shows the original stacked section from Baker (1999) with some additional gain applied and 4-6b) shows stacked section after f-k filter has been applied to increase lateral coherency (see Appendix B for different f-k filters applied). The horizontal axis in this figure is trace number and the spacing between the traces is 0.25 meters. The vertical axis is two-way reflection time down to 0.2 seconds, with the near surface speeds this corresponds to a depth of approximately 40 meters (Baker, 1999).

We again selected a particular trace, here trace 75, to display a spectrogram of the frequency content with time, and this is shown in Figure 4-7. As can be seen, the frequency content of the trace decreases with time. Figure 4-8 shows the CNS-ITD applied to this trace for different numbers of iterations. Figure 4-8a) shows the seismic trace along with the window functions, and 4-8b) shows the estimated propagating wavelets for each window. These are continuously interpolated as needed within the CNS-ITD iterative process. Figure 4-8c) shows the residual traces for different numbers of iterations along with the mean square error (MSE). After 20 iterations the MSE has decreased to around three percent. The resulting deconvolved reflectivities are shown in Figure 4-8d) for different numbers of iterations. Note that the estimated propagating wavelets are also normalized here, to obtain the trace amplitudes, which then can be enhanced by applying gain correction.

We then performed the CNS-ITD to each trace of the Kansas dataset. The resulting deconvolved reflectivities for each of the traces are then re-convolved with a stationary 100 Hz

Ricker wavelet. An f-k filter was applied slightly to increase the lateral coherency. Figure 4-9a) shows the seismic section from Figure 4-6b, and the result of CNS-ITD re-convolved with a stationary 100 Hz Ricker wavelet is shown in 4-9b). Results for different Ricker wavelets with different dominant frequencies are shown in Appendix D. It can be seen that the resolution has been improved by CNS-ITD particularly for greater times. This can be verified by the spectrogram of trace 75 after CNS-ITD re-convolved with a stationary 100 Hz Ricker wavelet which is shown in Figure 4-10. The spectrograms of trace 75 for different Ricker wavelets are also shown in Appendix D.

Table 4-1. Parameters and equipment used in collecting the Thames River dataset (from Baker, 1999).

Seismograph	Geometrics 2401
Receivers	24 100-Hz geophones
Source	Buffalo gun
Receiver spacing	2.5 m
Shot spacing	2.5 m
Record length	250 ms
Sampling interval	0.5 ms
Number of shots	20

Table 4-2. Parameters and equipment used in collecting Kansas dataset (from Baker, 1999).

Seismograph	BISON 24096
Receivers	96 100-Hz geophones
Source	30.06 rifle
Receiver spacing	0.5 m
Shot spacing	1 m
Record length	500 ms
Sampling interval	0.25 ms
Number of shots	74

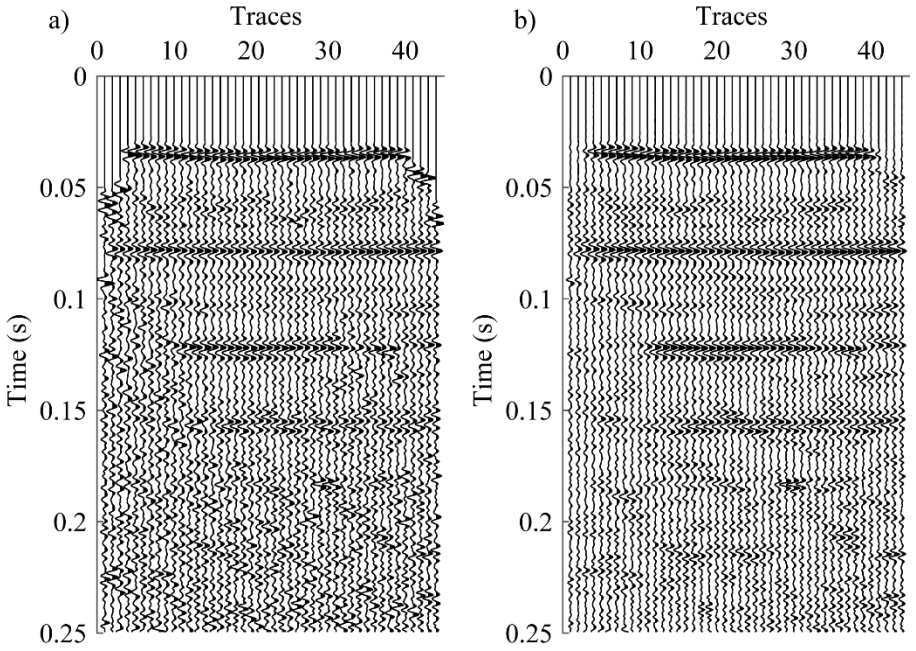

Figure 4-1. a) shows the original stacked section of the Thames River data from Baker (1999) and b) shows the seismic stacked section with f-k filtering applied using the parameters described in Appendix A.

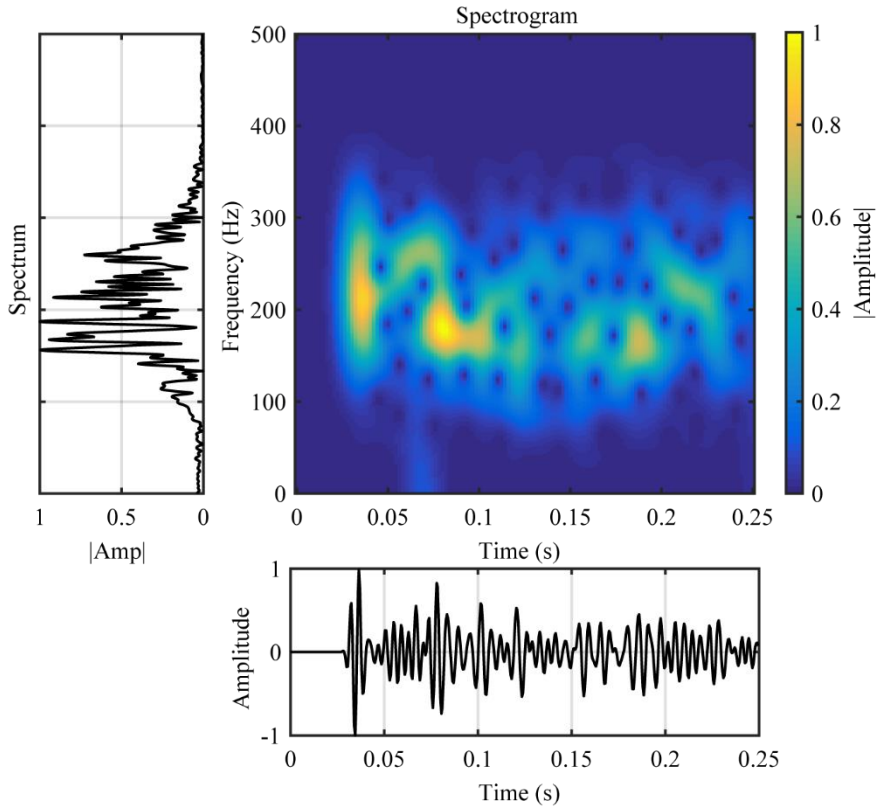

Figure 4-2. Spectrogram of trace 10 from the stacked seismic section of the Thames River dataset shown in Figure 4-1b). The non-stationary character of the seismic trace can be seen where the amplitudes of the spectrum show a decrease in frequency with time. The amplitudes on the spectrogram are enhanced for demonstration purposes.

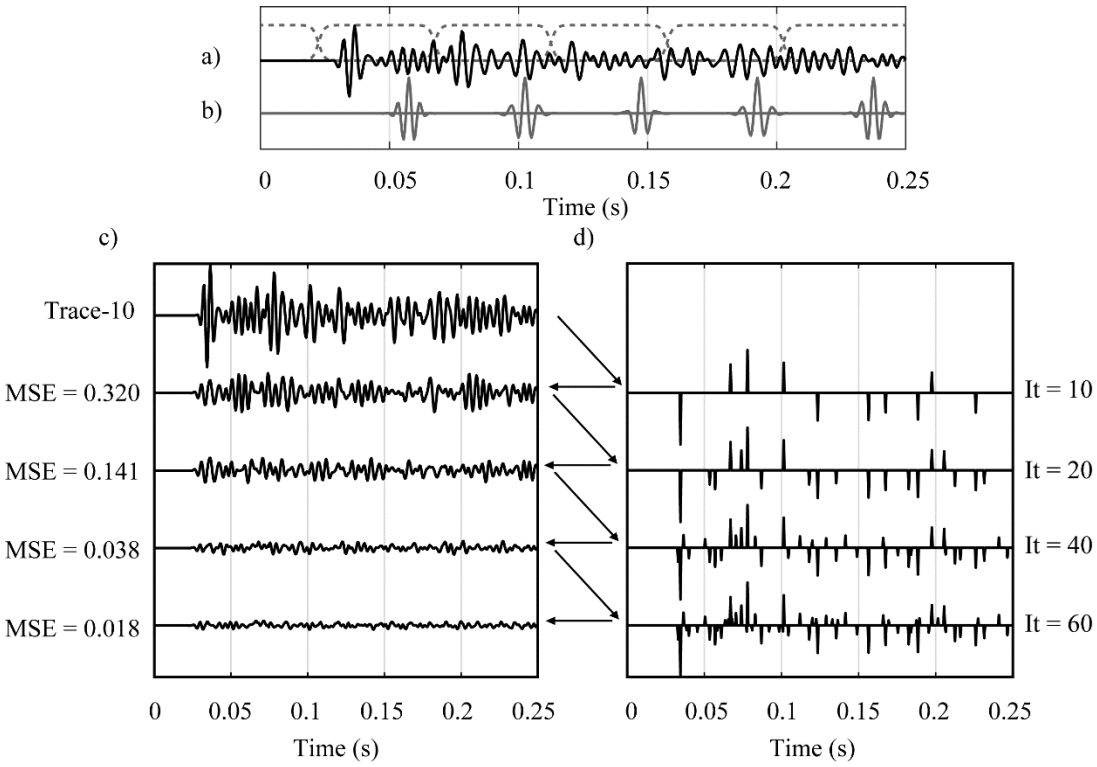

Figure 4-3. Shows an application of continuous non-stationary iterative time-domain deconvolution (CNS-ITD) to trace 10 from seismic section shown in Figure 4-1b). a) shows the seismic trace together with window functions, and b) shows the estimated propagating wavelets for each window. c) shows the trace 10 on the top and residual traces for different numbers of iterations specified by It, where It=10 signifies ten iterations have been performed on the trace and this produces the spike diagram shown in d). Similarly, the results for different numbers of iterations for the residual traces and the mean square errors (MSE) are shown in c).

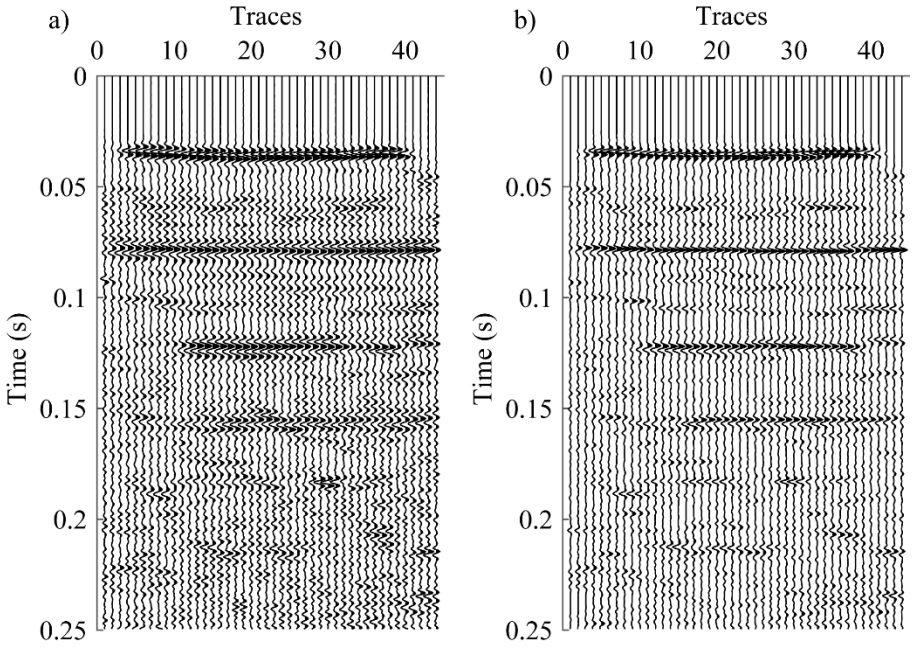

Figure 4-4. a) shows the stacked section from Figure 4-1b). b) shows the stacked seismic section after continuous nonstationary iterative time-domain deconvolution (CNS-ITD). The estimated reflectivity has been re-convolved with a stationary 250 Hz Ricker wavelet, and an f-k filter has been applied to slightly increase lateral coherence.

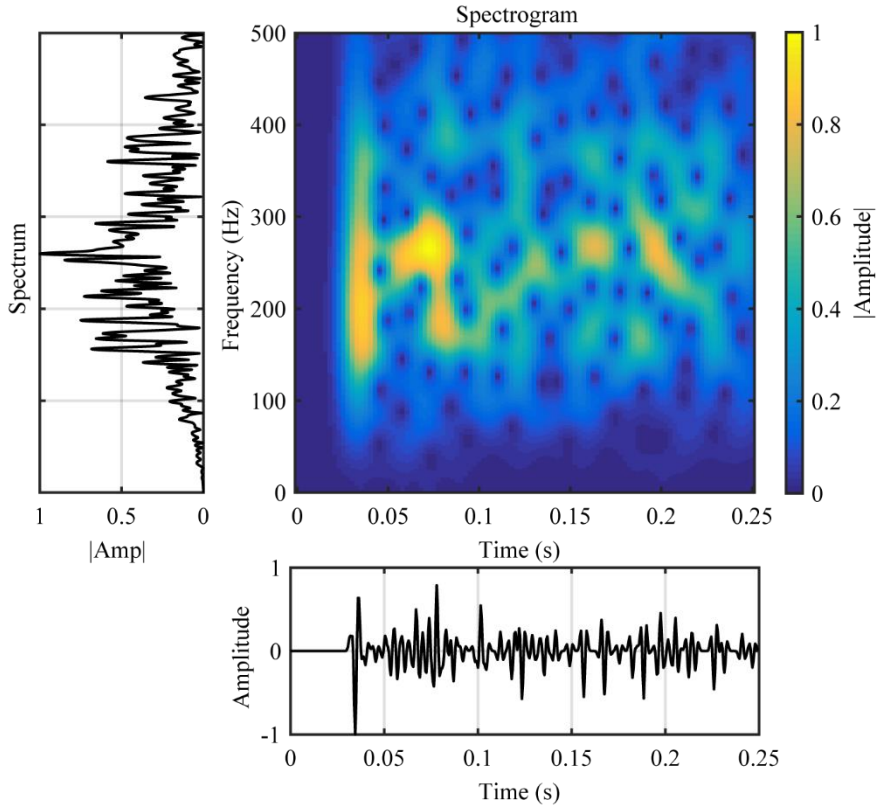

Figure 4-5. This figure shows the trace 10 after CNS-ITD and re-convolved with a stationary 250 Hz Ricker wavelet. Comparing with Figure 4-2, it can be seen from the seismic trace, the spectrum and the spectrogram that the frequency content has been increased and is more uniform with frequency after the deconvolution and re-convolution with a stationary 250 Hz Ricker wavelet. The amplitudes on the spectrogram are enhanced for demonstration purposes.

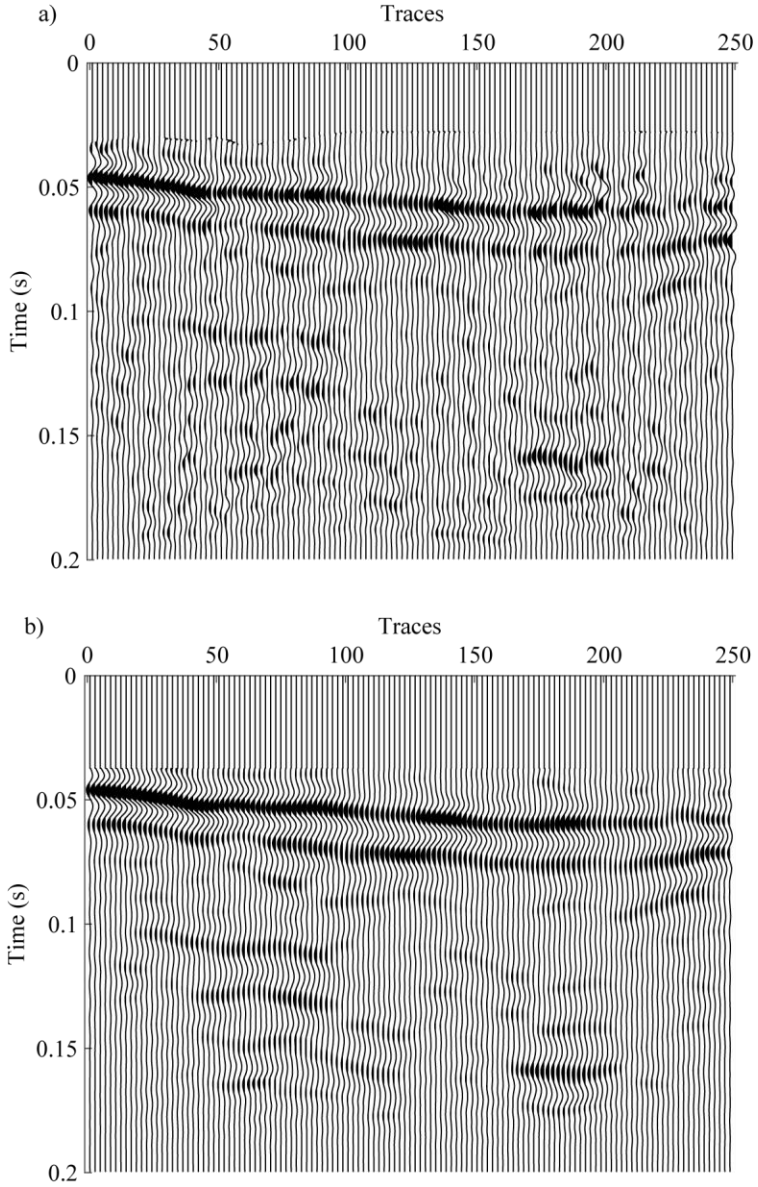

Figure 4-6. a) shows the original stacked seismic section of the Kansas dataset from Baker (1999) with an additional gain applied and b) shows the seismic stacked section with an f-k filter applied to increase lateral coherency.

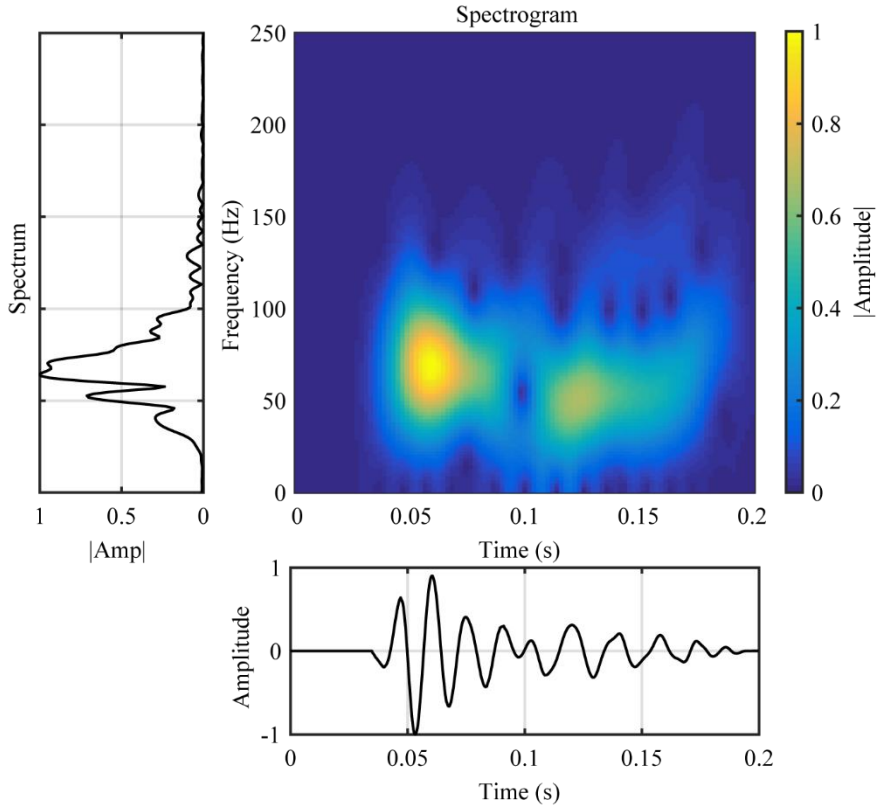

Figure 4-7. Spectrogram of trace 75 from the stacked seismic section of Kansas dataset from Baker (1999) shown in Figure 4-6b). The amplitudes on the spectrogram are enhanced for demonstration purposes. The non-stationary character of the seismic trace can be seen where the amplitudes of the spectrogram show a decrease in frequency with time.

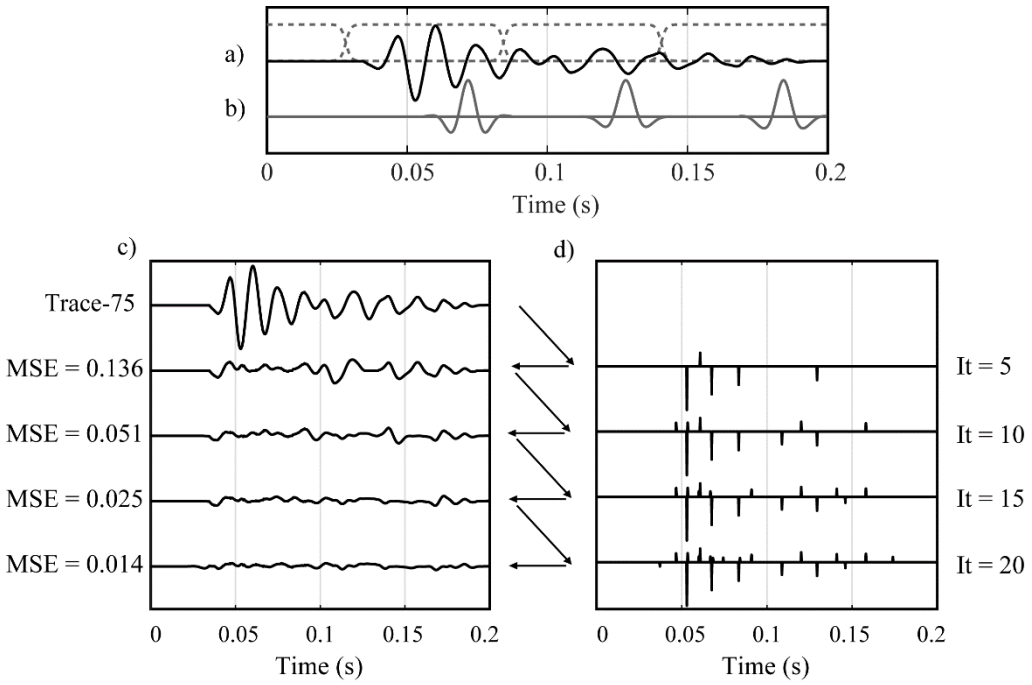

Figure 4-8. Shows an application of continuous non-stationary iterative time-domain deconvolution (CNS-ITD) to trace 75 from the stacked section of Kansas dataset shown in Figure 4-6b). a) shows the seismic trace together with window functions, and b) shows the estimated propagating wavelets for each window. c) shows trace 75 on the top and residual traces for different numbers of iterations specified by It, where It=5 signifies five iterations have been performed along the trace and this produces the spike diagram shown in d). Similarly, the results for different numbers of iterations are also shown in d), and the residual traces along with the mean square errors (MSE) are shown in c).

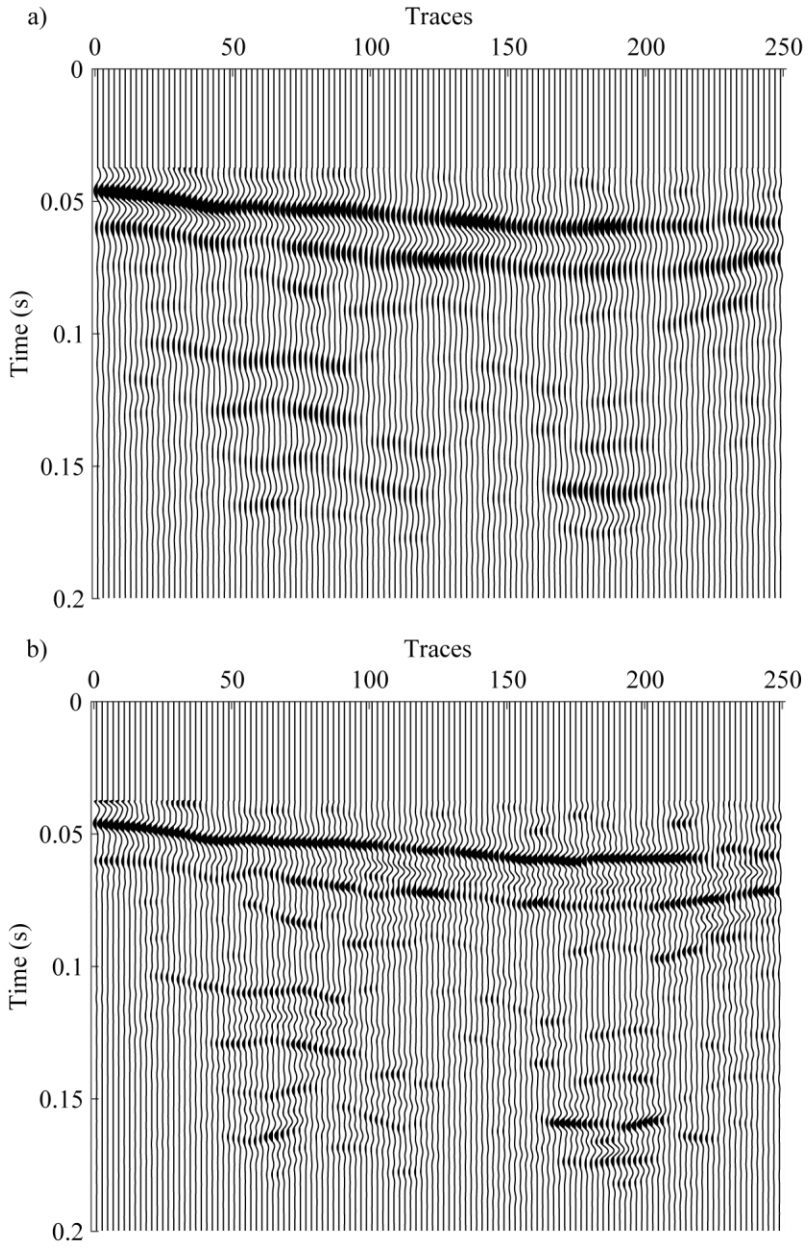

Figure 4-9. a) shows the stacked section from Figure 4-6b). b) shows the stacked section after CNS-ITD. An f-k filter has also been applied slightly to increase lateral coherence. The estimated reflectivity has been re-convolved with a stationary 100 Hz Ricker wavelet.

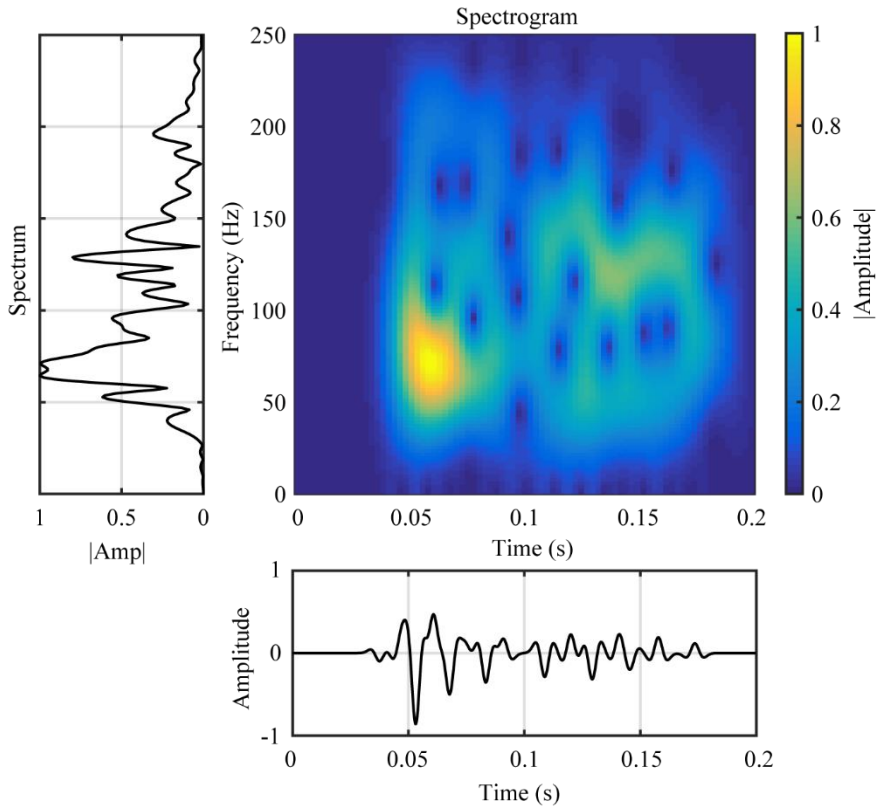

Figure 4-10. Spectrogram of trace 75 from the stacked seismic section of Kansas dataset after CNS-ITD and re-convolved with a stationary 100 Hz Ricker wavelet. The amplitudes on the spectrogram are enhanced for demonstration purposes.

CHAPTER 5. CONCLUSIONS

We have introduced an extension of iterative time-domain deconvolution to the non-stationary case and applied it to shallow seismic reflection data. The use of matrix-vector operations have allowed us to perform non-stationary iterative deconvolution operations continuously along the seismic trace. By dividing the trace into several overlapping windows, the propagating wavelets can be estimated in each sub-window. The selected set of propagating wavelets are then interpolated as required within the continuous non-stationary iterative time-domain deconvolution (CNS-ITD) process. The estimated propagating wavelets are then assigned to the specific columns of the non-stationary $\boldsymbol{S}$ matrix and used within the CNS-ITD.

We have tested CNS-ITD on both synthetic and observed data. For the synthetic data, we were able to estimate the reflectivities with high accuracy. Note that for a minimum phase wavelet, the time shift described earlier should be compensated to accurately locate the reflectivity. For zero phase wavelet, there is no time-shift involved in the process. We then applied CNS-ITD to two observed shallow seismic reflection datasets. Since the datasets used here have been already processed, we assumed that the estimated propagating wavelets are zero-phase. Applying CNS-ITD to these observed data have successfully recovered higher frequencies in the data by removing attenuation and scattering effects, and compressing the propagating wavelets, resulting in higher-resolution in the shallow seismic data.

REFERENCES

Baker, G.S., Steeples, D.W. & Drake, M., 1998. Muting the noise cone in near-surface reflection data: An example from southeastern Kansas: *Geophysics*, **63**, 1332-1338.

Baker, G.S., 1999. Processing Near-Surface Seismic-Reflection Data: A Primer, Society of Exploration Geophysics (SEG), Tulsa, OK.

Grossman, J.P., Margrave G.F. & Lamoureux, M.P., 2002. Constructing adaptive, nonuniform Gabor frames from partitions of unity, *CREWES Research Report*, **14**, 1–10, University of Calgary, Canada.

Hale, D., 1981. An Inverse-Q filter: Stanford Exploration Project Report, **26**, 133–158.

Hargreaves, N.D., 1992. Air-gun signatures and the minimum-phase assumption, *Geophysics*, **57**, 263-271.

Kikuchi, M. & Kanamori, H., 1982. Inversion of complex body waves, *Bull. Seism. Soc. Am.*, **72**, 491-506.

Kjartansson E., 1979. Constant Q wave propagation and attenuation. *Journal of Geophysical Research*, **84**, 4737-4748.

Lari, H.H. & Gholami A., 2019. Nonstationary blind deconvolution of seismic records, *Geophysics*, **84**, V1-V9.

Ligorria, J.P. & Ammon, C.J., 1999. Iterative deconvolution and receiver-function estimation, *Bull. Seismol. Soc. Am.*, **89**, 1395–1400.

Margrave, G.F., 1998. Theory of nonstationary linear filtering in the Fourier domain with application to time variant filtering, *Geophysics*, **63**, 244-259.

Margrave, G.F., & Lamoureux, M.P., 2001. Gabor deconvolution, *CREWES Research Report*, **13**, 241–276, University of Calgary, Canada.

Margrave, G.F., Gibson, P.C., Grossman, J.P., Henley, D.C., Iliescu V., & Lamoureux, M.P., 2005. The Gabor transform, pseudodifferential operators, and seismic deconvolution. *Integrated Computer-Aided Engineering*, ***12***, 43-55.

Margrave, G.F., Lamoureux, M.P., & Henley, D.C., 2011. Gabor deconvolution: Estimating reflectivity by nonstationary deconvolution of seismic data, *Geophysics*, **76**(3), W15–W30.

Margrave, G.F., & Lamoureux, M.P., 2019. Numerical Methods of Exploration Seismology: With Algorithms in MATLAB**,** *Cambridge University Press.*

Morozov, I.B, Haiba, M., & Deng, W., 2018. Inverse attenuation filtering, *Geophysics*, **83**, V135-V147.

Robinson, E.A., 1966. Multichannel z-transforms and minimum-delay, *Geophysics*, **31**, 482-500.

Robinson E.A., 1967. Predictive decomposition of time series with application to seismic exploration, *Geophysics*, **32**, 418-484.

Robinson E.A., & Osman O.M., (eds.), 1996. Deconvolution 2, *Geophysics Reprint Series*, **17**, Society of Exploration Geophysics (SEG), Tulsa, OK.

Steeples, D.W., 2005. Shallow seismic methods, in *Hydrogeophysics* (Eds. Y. Rubin and S. S. Hubbard, Springer, 185–213.

Wang, Y., 2002. A stable and efficient approach of inverse Q filtering, *Geophysics*, **67**, 657–663.

Wang, Y., 2006. Inverse Q-filter for seismic resolution enhancement, *Geophysics*, **71**, V51–V60.

Wang, Y., 2008. Seismic inverse Q filtering, *Wiley-Blackwell.*

Webster, G.M, (Ed.), 1978. Deconvolution. Vols. 1 and 2, Society of Exploration Geophysics (SEG), Tulsa, OK.

Yilmaz, O., 2001. Seismic data processing. Vols. 1 and 2, Society of Exploration Geophysics (SEG), Tulsa, OK.

APPENDIX A. ADDITIONAL F-K FILTERING RESULTS OF THE THAMES RIVER DATASET

To increase lateral coherency, f-k filtering can be applied. It is generally used to separate out seismic events that have different apparent velocities which are represented by different slopes in the f-k spectrum. The main parameter in the f-k filter is the slope of the seismic arrivals on the seismic section, which is inversely proportional to the apparent velocity on the f-k plot

$$\frac{df}{dk} = \frac{1}{V_{app}}.$$

F-k filtering has some pitfalls in its application. If too much is applied, it can overly reduce more steeply dipping events, and overemphasize horizontal events. It should be used properly, otherwise it can produce results which can be easily misinterpreted. Figure A-1a) shows the stacked section of the Thames river dataset processed by Baker (1999) and A-1b) shows f-k spectrum of this seismic section. Here, horizontal axis is the wavenumber (k) in units of 1/m, and vertical axis is the frequency in Hz. This dataset includes several nearly horizontal seismic reflections, and these are located around the k=0 axis. Incoherent seismic events which have widely different slopes can be filtered out from the seismic section by specifying the band of the apparent velocities. Figure A-2a) shows the f-k filtered stacked section. Here, we filtered out the velocity band ranging from infinitely high velocities with a slope = 0.000 to 0.0001 s/m (apparent velocity band from 0 to 1000 m/s). The resulting stack section includes less noise and shows more lateral coherence between the seismic traces. Figure A-3, and A-4 shows filtered stacked sections by using different velocity bands. In observed data applications part, the data that is filtered using the apparent velocity band from 0 to 1500 m/s is used, which is shown in Figure A-3.

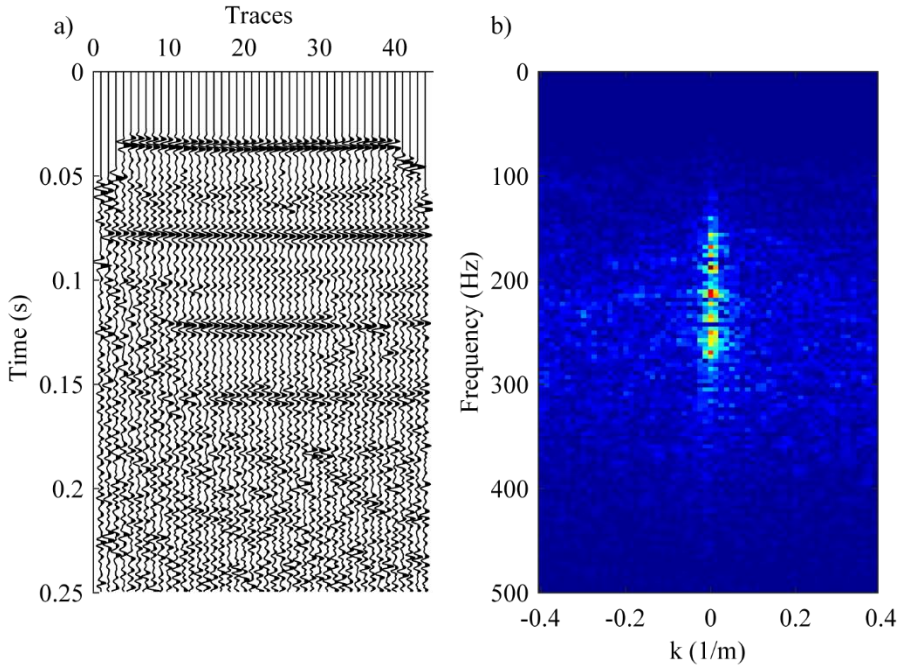

Figure A-1. a) shows the original stacked section of the Thames River dataset from Figure 4-1a). b) shows the f-k spectrum of these data.

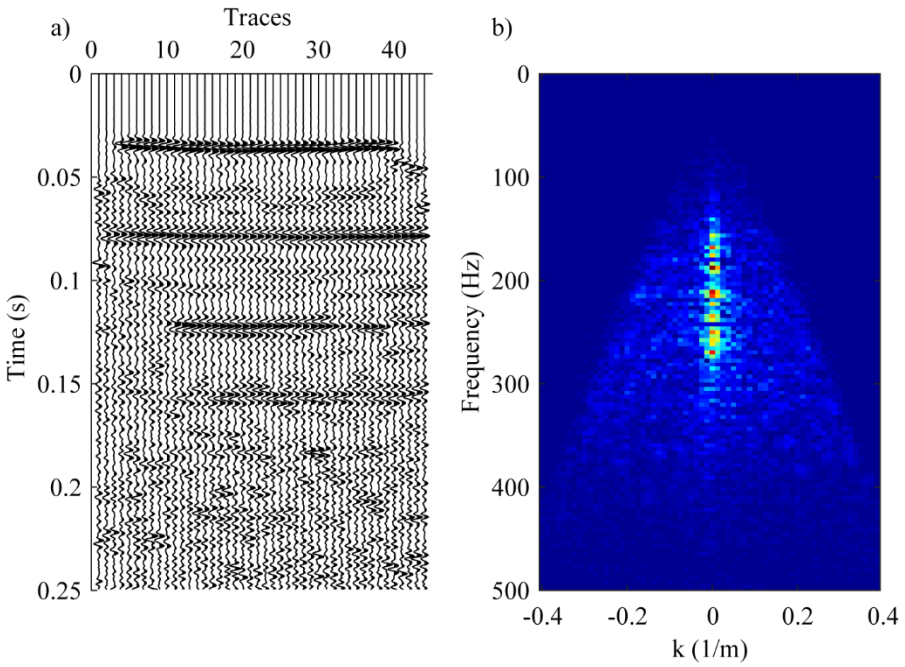

Figure A-2. a) shows the stacked section that f-k filter was applied by using the band of velocities starting from 0 to 1000 m/s. b) shows the f-k spectrum of the filtered stacked section.

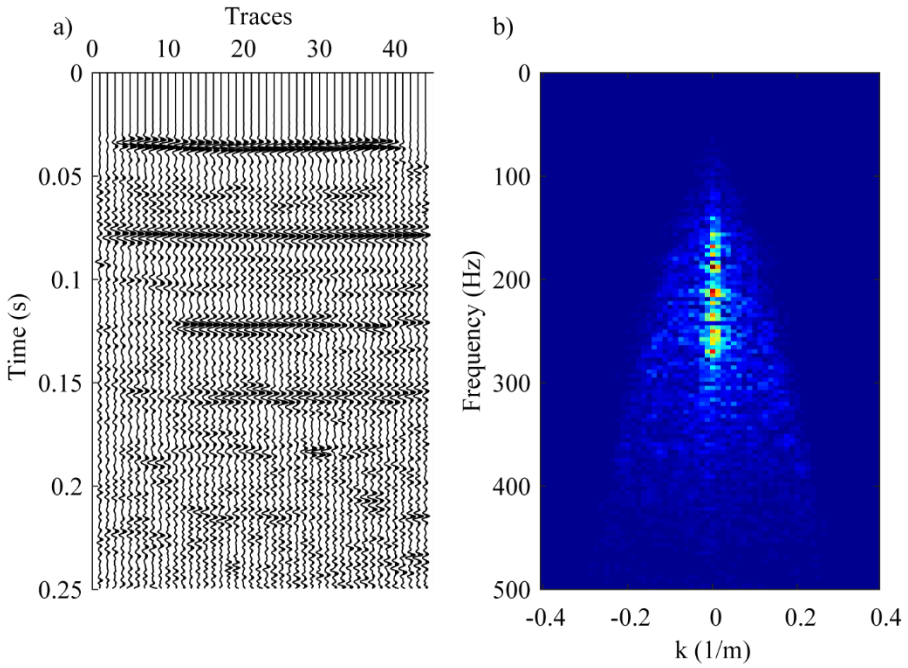

Figure A-3. a) shows the stacked section that f-k filter was applied by using the band of velocities starting from 0 to 1500 m/s. b) shows the f-k spectrum of the filtered stacked section.

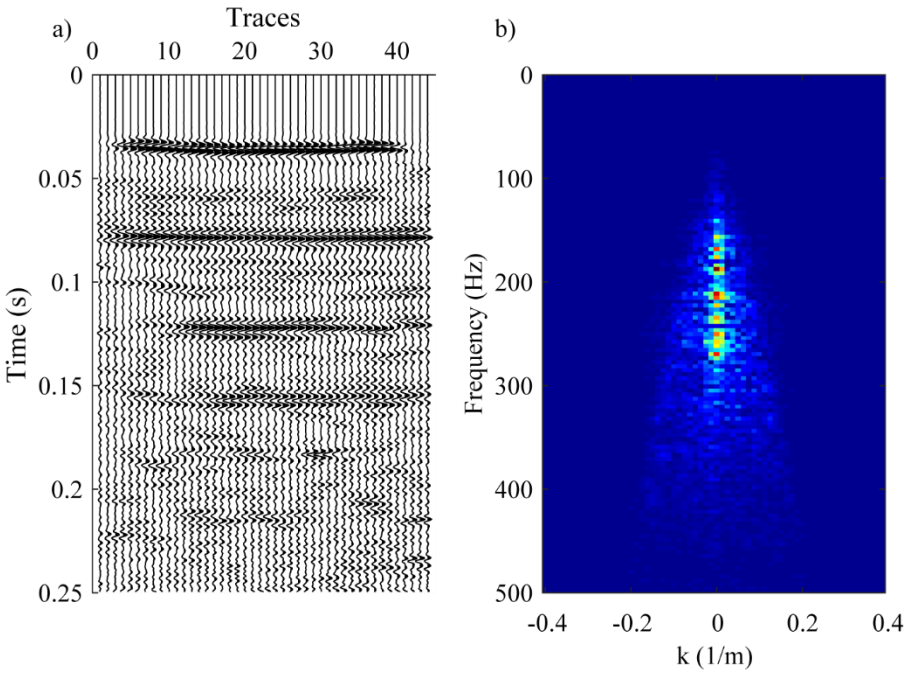

Figure A-4. a) shows the stacked section that f-k filter was applied by using the band of velocities starting from 0 to 2000 m/s. b) shows the f-k spectrum of the filtered stacked section.

APPENDIX B. ADDITIONAL RESULTS FOR THE THAMES RIVER DATASET USING DIFFERENT DOMINANT FREQUENCY RICKER WAVELETS

After continuous non-stationary iterative time-domain deconvolution (CNS-ITD) of all the seismic traces in Figure 4-1b), Figure B-1b) shows the deconvolved reflectivities for each of the traces obtained from the stacked section B-1a). These estimated reflectivities can then be re-convolved with a higher frequency stationary wavelet. Figure 4-2 shows the spectrogram for trace-10, and Figure B-2 shows the spectrogram of the estimated reflectivities for trace-10 where the frequency content has been increased. Since the dominant frequency in Thames River data is around 200 Hz, we can use a stationary wavelet with a dominant frequency of 200 Hz and above to re-convolve the estimated reflectivities. Figure B-3a) shows the seismic section from Figure 4-1b), and B-3b) shows the deconvolved reflectivities shown in Figure B-1b) which have been re-convolved with a stationary 200 Hz Ricker wavelet. Figure B-4 shows the spectrogram of the deconvolved trace 10 after being re-convolved with a 200 Hz Ricker wavelet. The Figures B-5a) and B-7a) shows the seismic sections from Figure 4-1b), and B-5b) and B-7b) shows the seismic sections that were re-convolved with 250 Hz and 300 Hz Ricker wavelets, respectively. The spectrograms of trace-10 for each case are also shown in Figure B-6 and B-8.

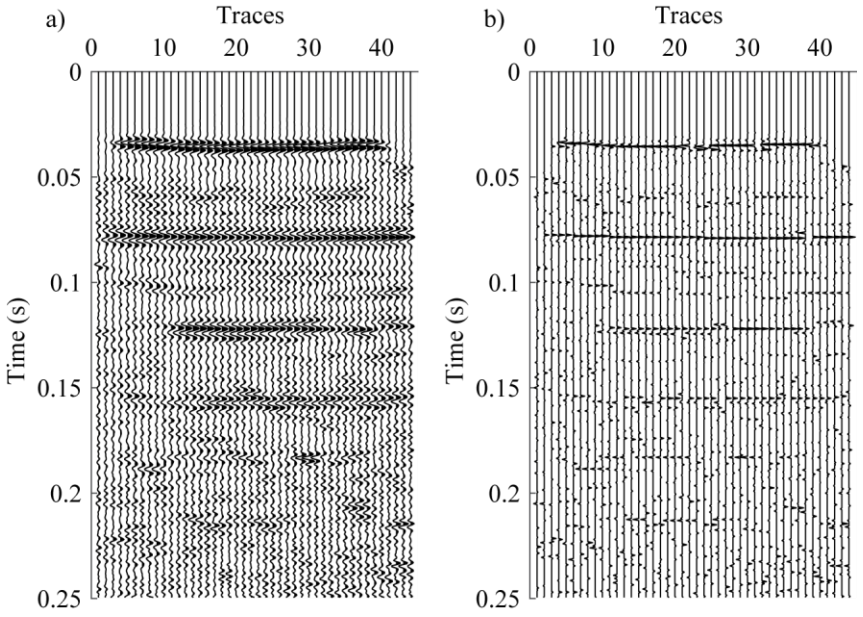

Figure B-1. a) shows the stacked section from Figure 4-1b). b) shows the estimated reflectivities after continuous non-stationary iterative time-domain deconvolution (CNS-ITD).

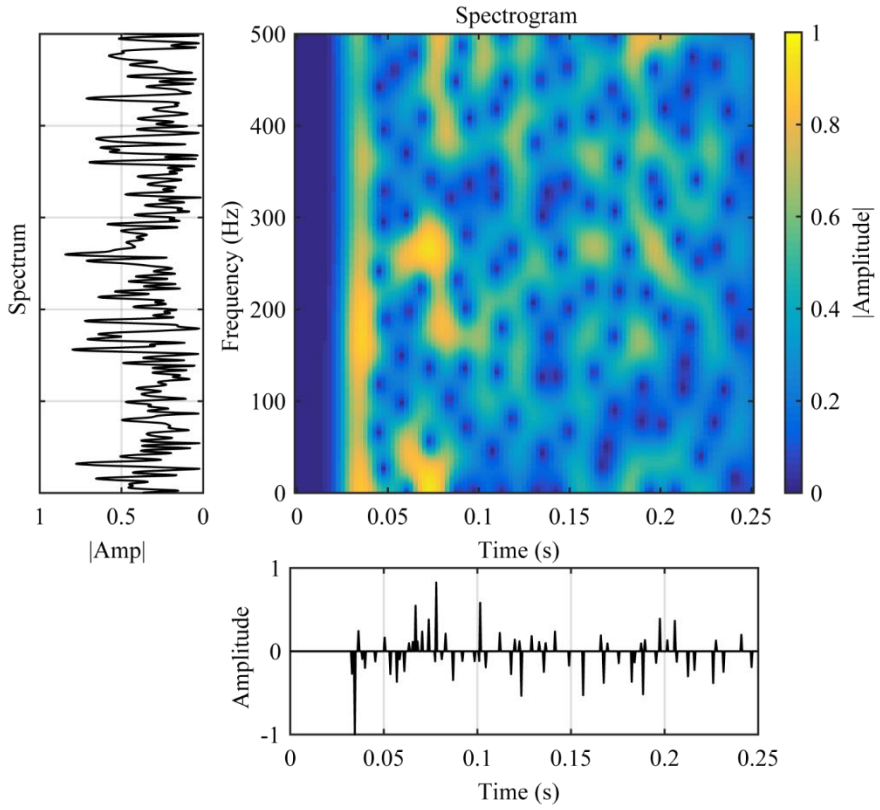

Figure B-2. This figure shows the estimated reflectivities and spectrogram for trace 10 after continuous non-stationary iterative time-domain deconvolution (CNS-ITD) has been applied shown in Figure B-1b).

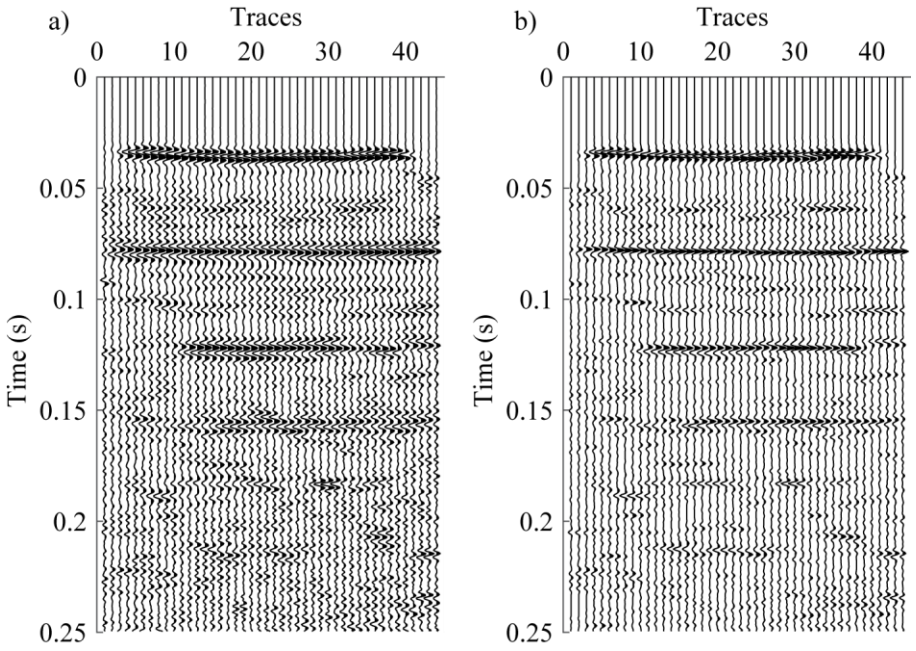

Figure B-3. a) shows the stacked section from Figure 4-1b). b) shows the CNS-ITD results. The estimated reflectivities shown in Figure B-1b) are here re-convolved with a stationary 200 Hz Ricker wavelet.

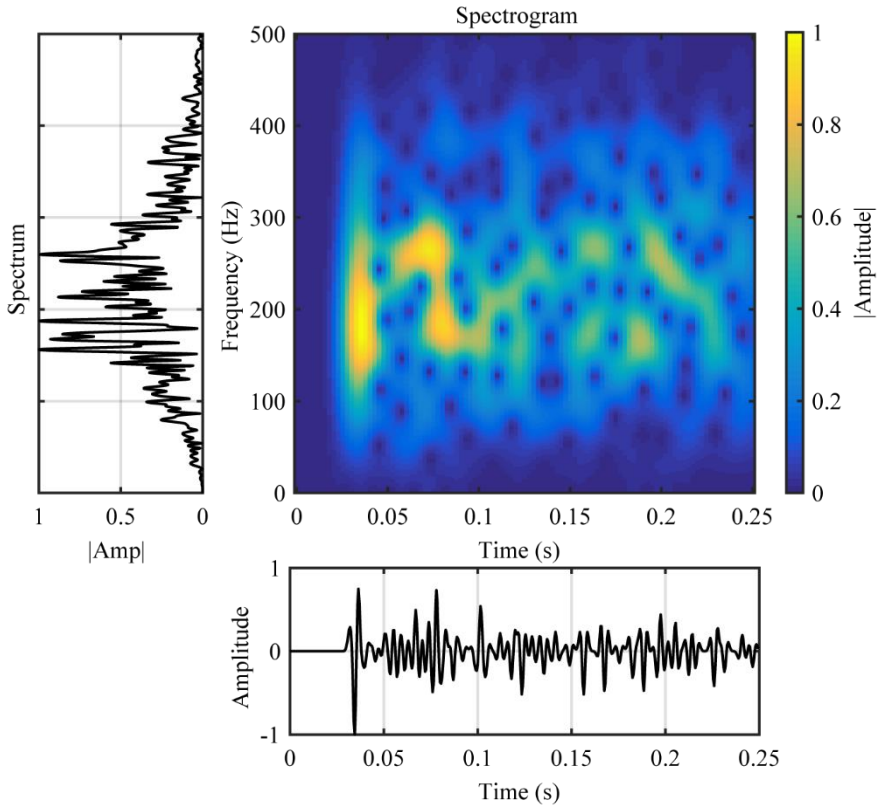

Figure B-4. This figure shows the trace 10 after CNS-ITD is applied shown in figure B-3b). Note that the estimated reflectivities shown in Figure B-1b) are re-convolved with a stationary 200 Hz Ricker wavelet.

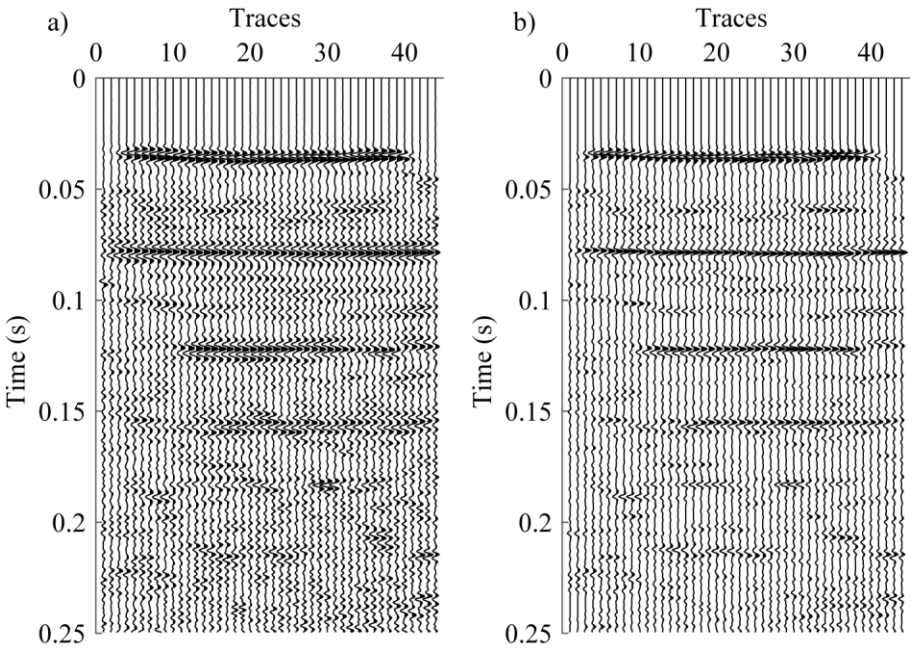

Figure B-5. a) shows the stacked section from Figure 4-1b). b) shows the CNS-ITD results. The estimated reflectivities shown in Figure B-1b) are here re-convolved with a stationary 250 Hz Ricker wavelet.

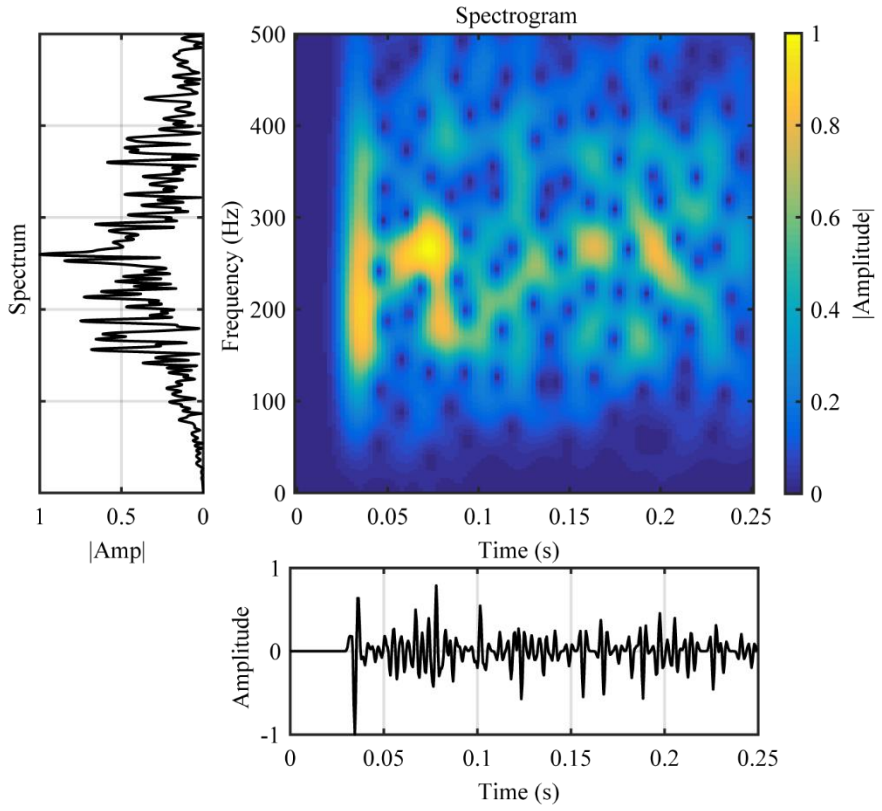

Figure B-6. This figure shows the trace 10 after CNS-ITD is applied shown in figure B-5b). Note that the estimated reflectivities shown in Figure B-1b) are re-convolved with a stationary 250 Hz Ricker wavelet.

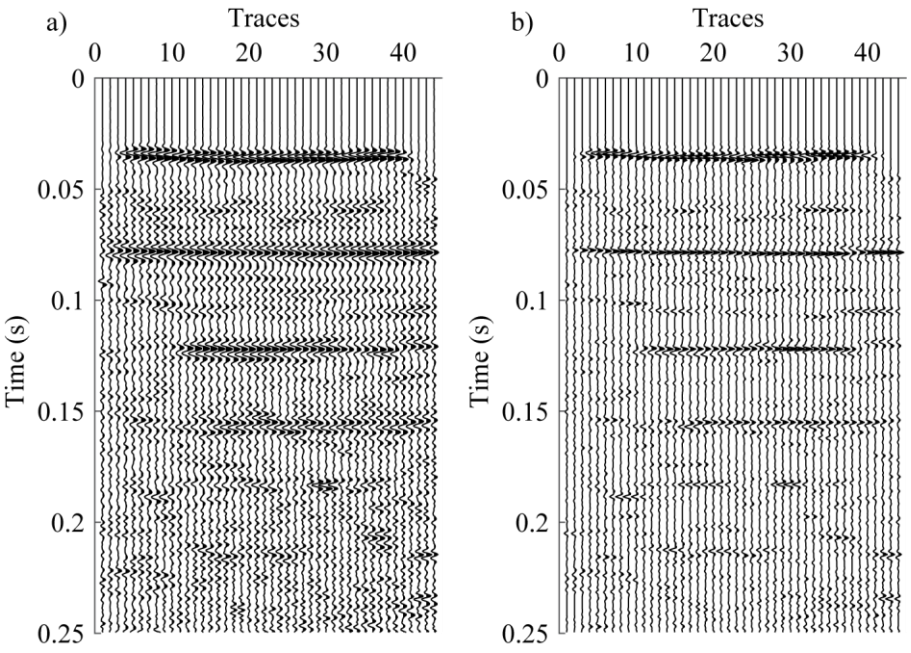

Figure B-7. a) shows the stacked section from Figure 4-1b). b) shows the CNS-ITD results. The estimated reflectivities shown in Figure B-1b) are here re-convolved with a stationary 300 Hz Ricker wavelet.

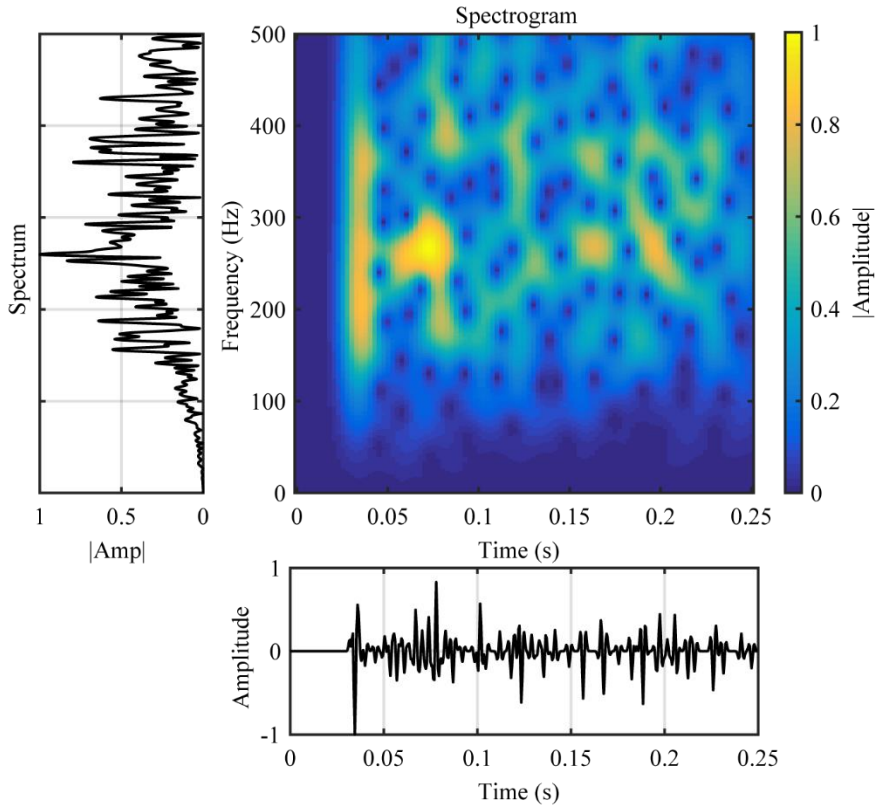

Figure B-8. This figure shows the trace 10 after CNS-ITD is applied shown in figure B-7b). Note that the estimated reflectivities shown in Figure B-1b) are re-convolved with a stationary 300 Hz Ricker wavelet.

APPENDIX C. ADDITIONAL F-K FILTERING RESULTS OF THE KANSAS DATASET

Figure C-1a) shows the Kansas dataset from Baker (1999) shown in Figure 4-6a) with a further gain correction applied. An f-k filter was then applied to this dataset which can be seen from the f-k spectrum shown in C-1b). However, some undesired seismic events are still present in the seismic section. To make the seismic section clearer, an additional f-k filter is applied to this dataset described in Appendix-A. Figure C-2a) shows the stacked section with an additional f-k filter applied by filtering the band of apparent velocities from 0 to 200 m/sec, which corresponds to slopes 0 to 0.005. Also, the f-k spectrum of the filtered seismic stacked section is shown in Figure C-2b). Figure C-3, and C-4 which is used in main text, show filtered stacked sections by filtering different apparent velocity bands together with the f-k spectrums.

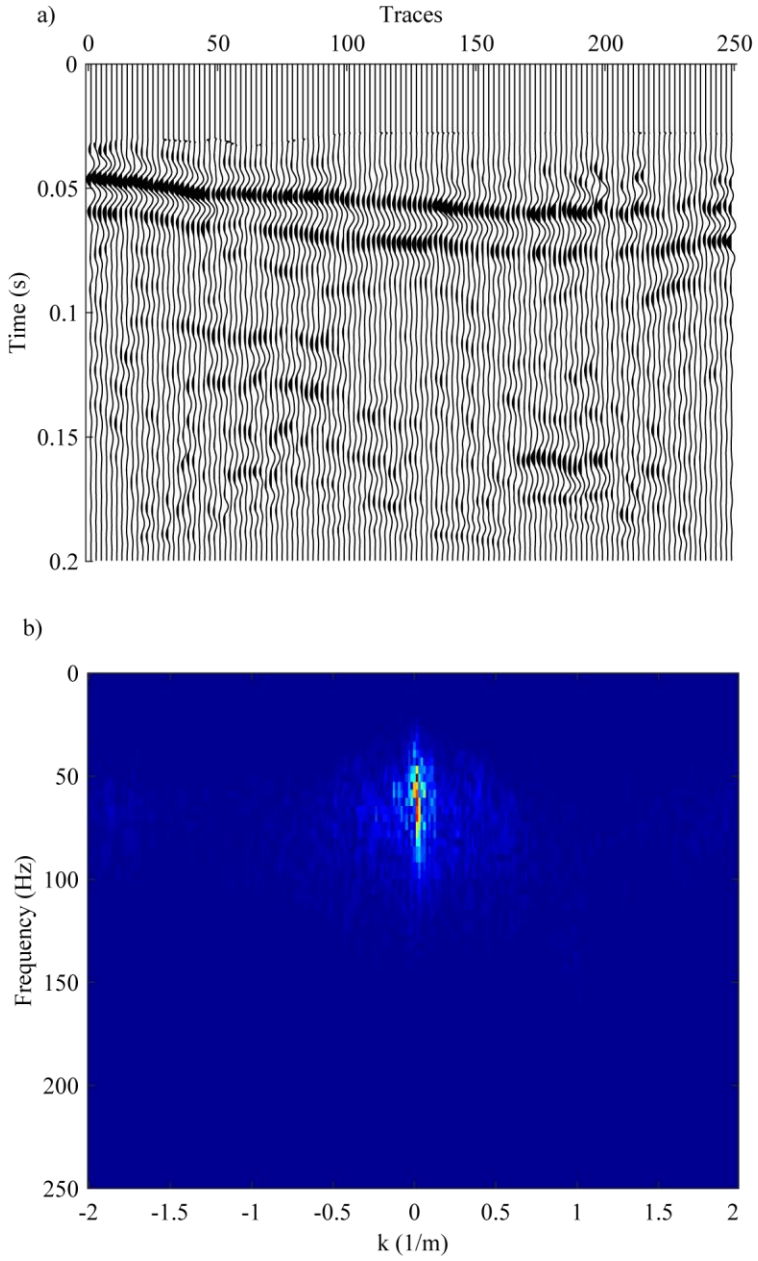

Figure C-1. a) shows the stacked section of the Kansas dataset from Baker (1999) shown in Figure 4-6a) with a further gain correction and b) shows the f-k spectrum of these data.

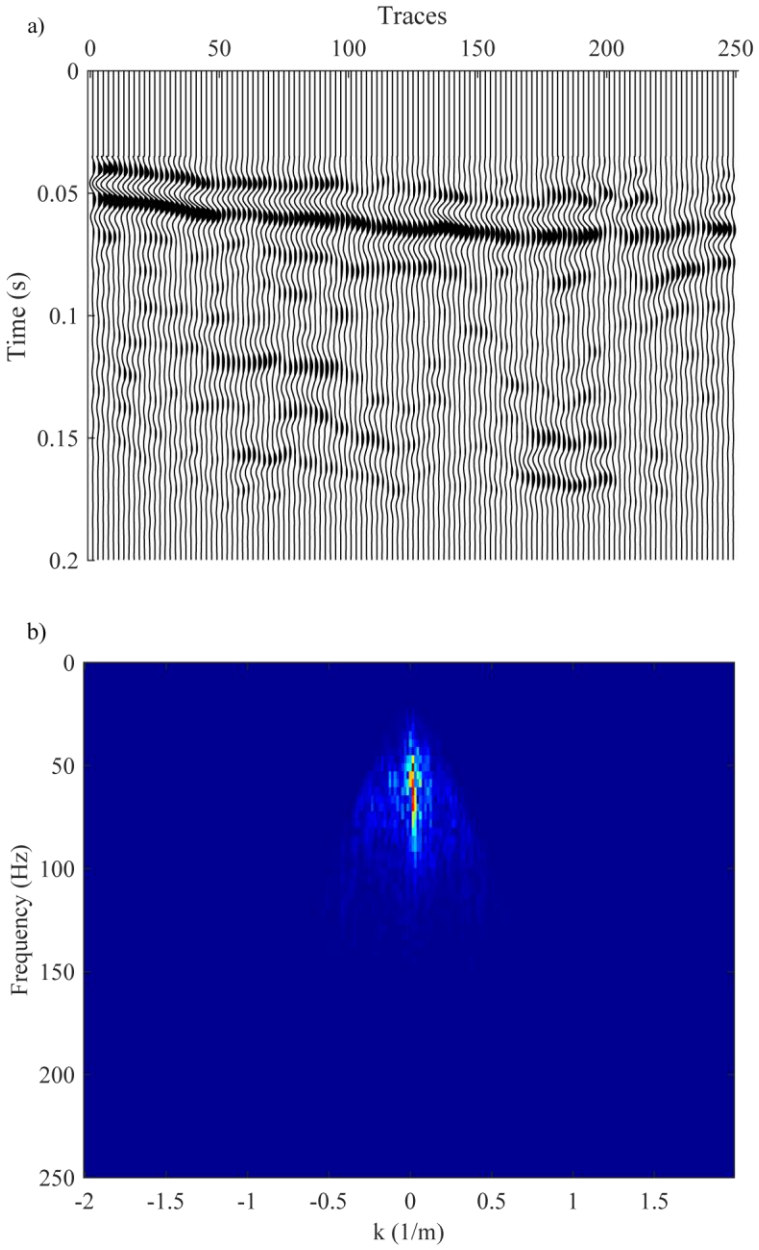

Figure C-2. a) shows the stacked section from the Figure C-1a) with an f-k filter applied using the band of velocities starting from 0 to 200 m/sec. b) shows the f-k spectrum of the filtered stacked section.

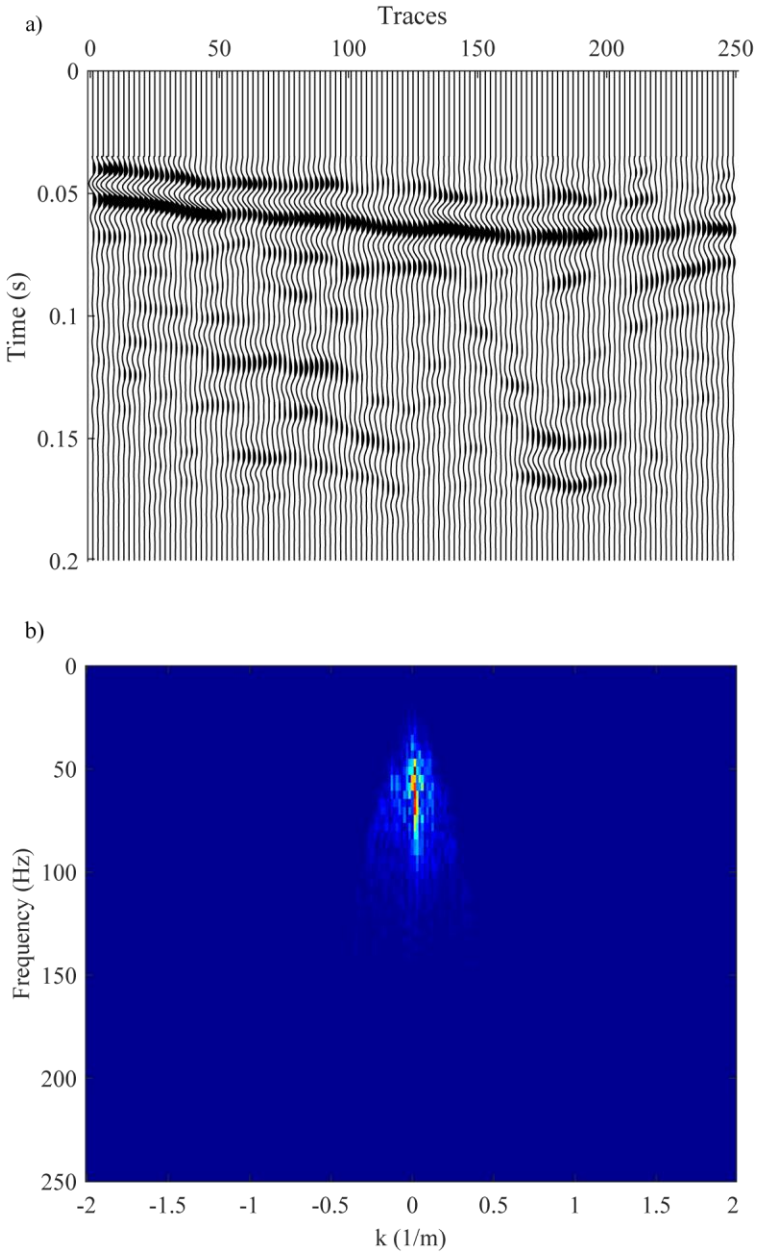

Figure C-3. a) shows the stacked section from the Figure C-1a) with an f-k filter applied using the band of velocities starting from 0 to 300 m/sec. b) shows the f-k spectrum of the filtered stacked section.

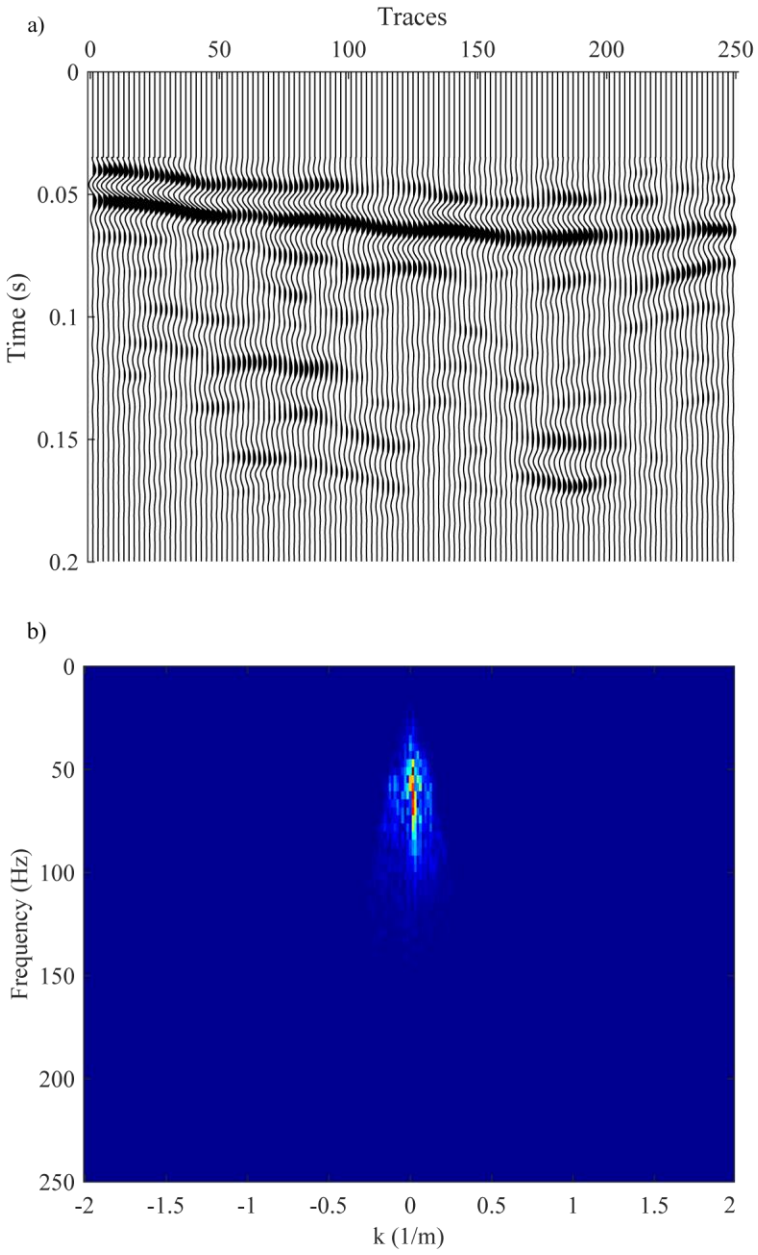

Figure C-4. a) shows the stacked section from the Figure C-1a) with an f-k filter applied using the band of velocities starting from 0 to 400 m/sec. b) shows the f-k spectrum of the filtered stacked section.

APPENDIX D. ADDITIONAL RESULTS FOR THE KANSAS DATASET USING DIFFERENT DOMINANT FREQUENCY RICKER WAVELETS

After continuous non-stationary iterative time-domain deconvolution (CNS-ITD) of all the seismic traces in Figure 4-6b), Figure D-1b) shows the deconvolved reflectivities for each of the traces obtained from the stacked section Figure D-1a). These estimated reflectivities can then be re-convolved with a higher frequency stationary wavelet. Figure D-2 shows the spectrogram of the estimated reflectivities for trace 75. The dominant frequency in Kansas data is around 70 Hz. Thus, we can use a stationary Ricker wavelet with dominant frequencies of 70 Hz and above to re-convolve the estimated reflectivities. Figure D-3a) shows the seismic section from Figure 4-6b), and D-3b) shows the deconvolved reflectivities which is shown in Figure D-1b) were re-convolved with a stationary 90 Hz Ricker wavelet to obtain the seismic section. The Figures D-5a) and D-7a) shows the seismic sections from Figure 4-1b), and D-5b) and D-7b) shows the seismic sections that were re-convolved with 80 Hz and 100 Hz Ricker wavelets, respectively. The spectrograms of trace 75 for each case are also shown in Figure D-6 and D-8.

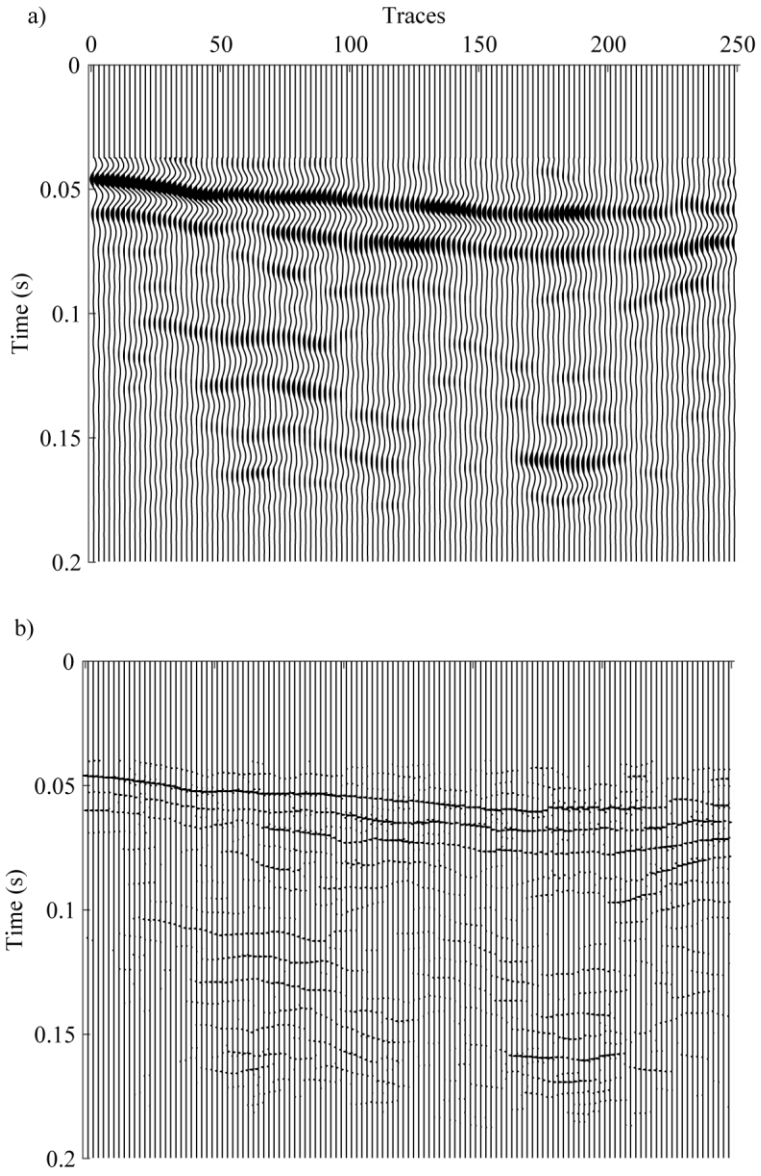

Figure D-1. a) shows the stacked section from Figure 4-6b). b) shows the estimated reflectivities after continuous non-stationary iterative time-domain deconvolution (CNS-ITD).

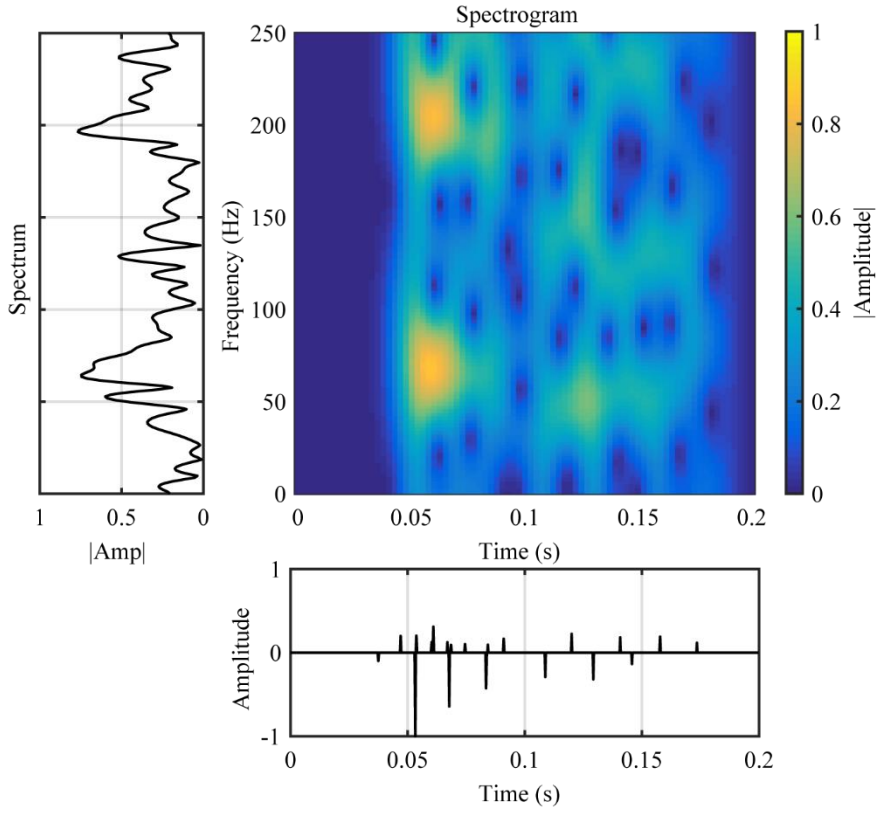

Figure D-2. This figure shows the estimated reflectivities and spectrogram of these for trace 75 after continuous non-stationary iterative time-domain deconvolution application shown in Figure D-1b).

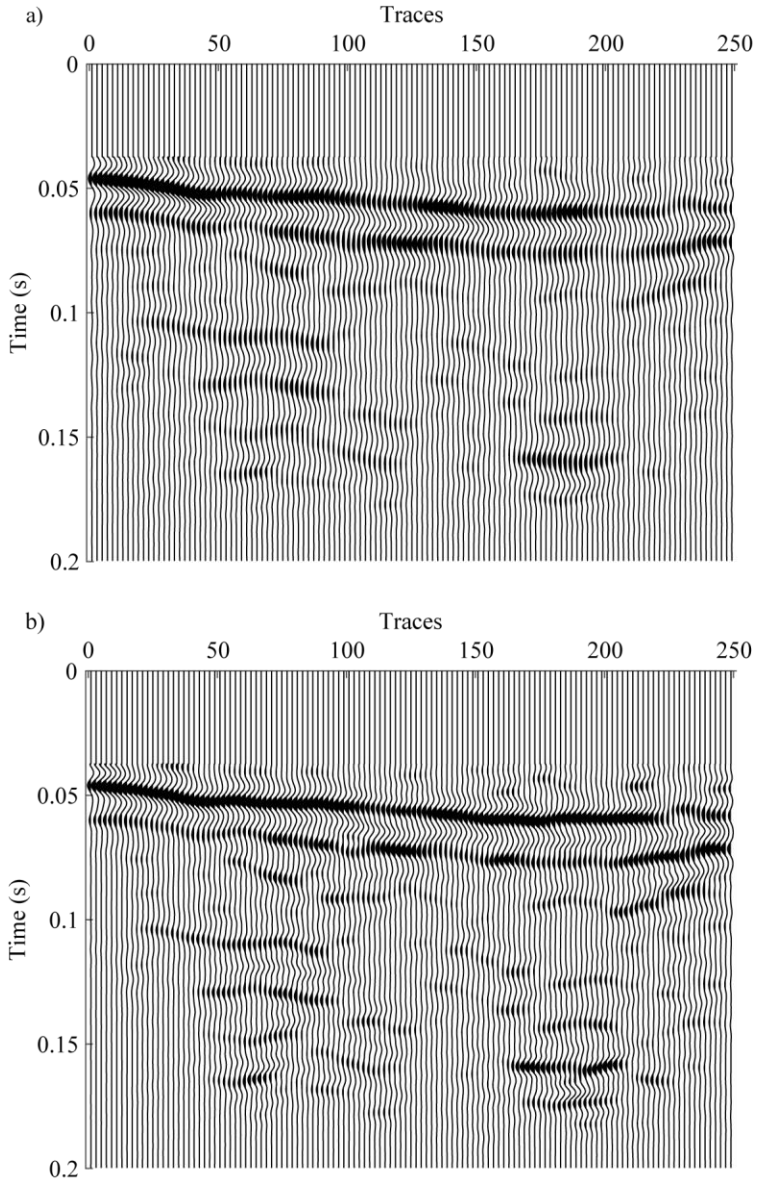

Figure D-3. a) shows the stacked section from Figure 4-6b). b) shows the CNS-ITD results. The estimated reflectivities shown in Figure D-1b) are here re-convolved with a stationary 80 Hz Ricker wavelet.

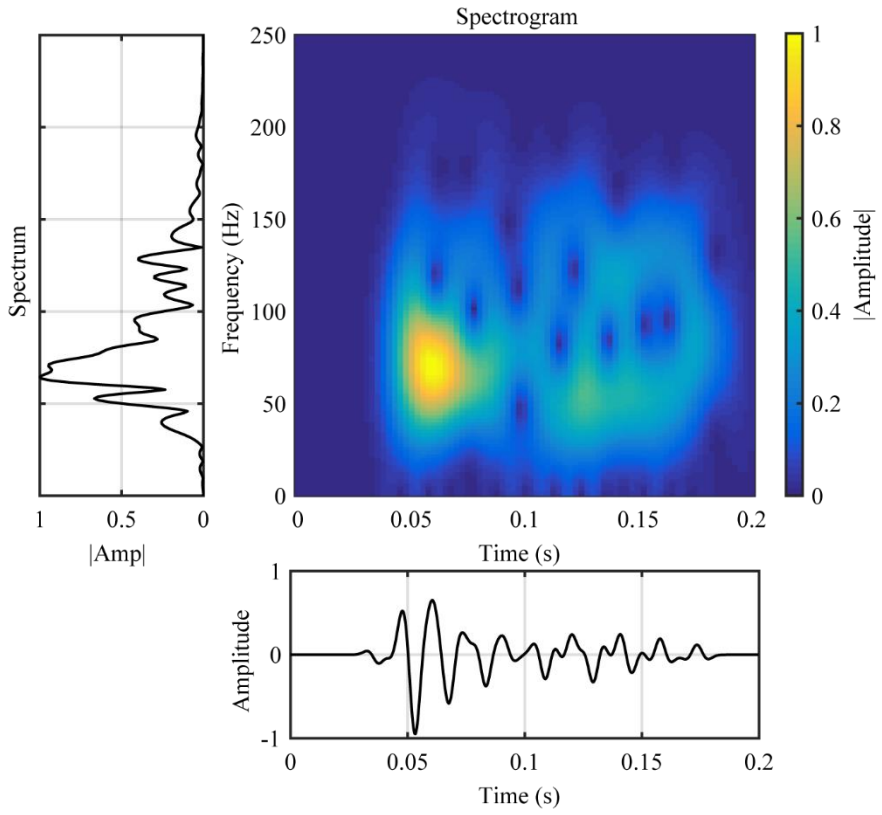

Figure D-4. This figure shows the trace 75 after CNS-ITD is applied shown in figure D-3b). Note that the estimated reflectivities shown in Figure B-1b) are re-convolved with a stationary 80 Hz Ricker wavelet. The amplitudes on the spectrogram are enhanced for demonstration purposes.

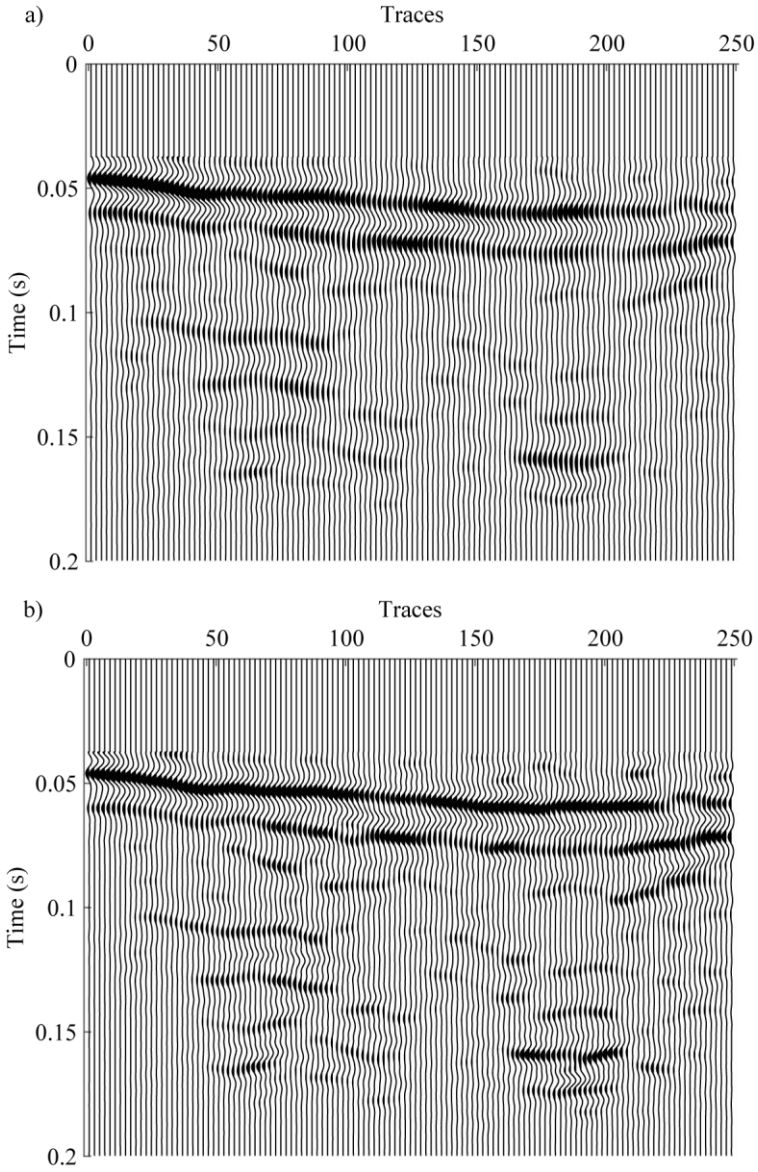

Figure D-5. a) shows the stacked section from Figure 4-6b). b) shows the CNS-ITD results. The estimated reflectivities shown in Figure D-1b) are re-convolved with a stationary 90 Hz Ricker wavelet.

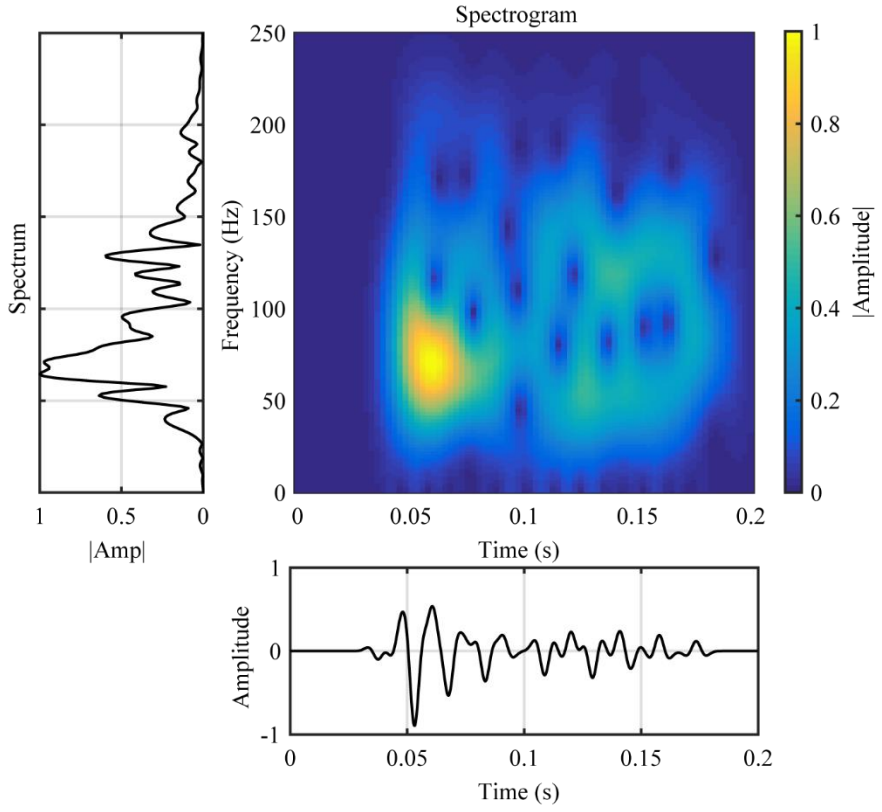

Figure D-6. This figure shows the trace 75 after CNS-ITD application shown in figure D-5b). Note that the estimated reflectivities for trace 75 shown in Figure D-1b) are re-convolved with a stationary 90 Hz Ricker wavelet.

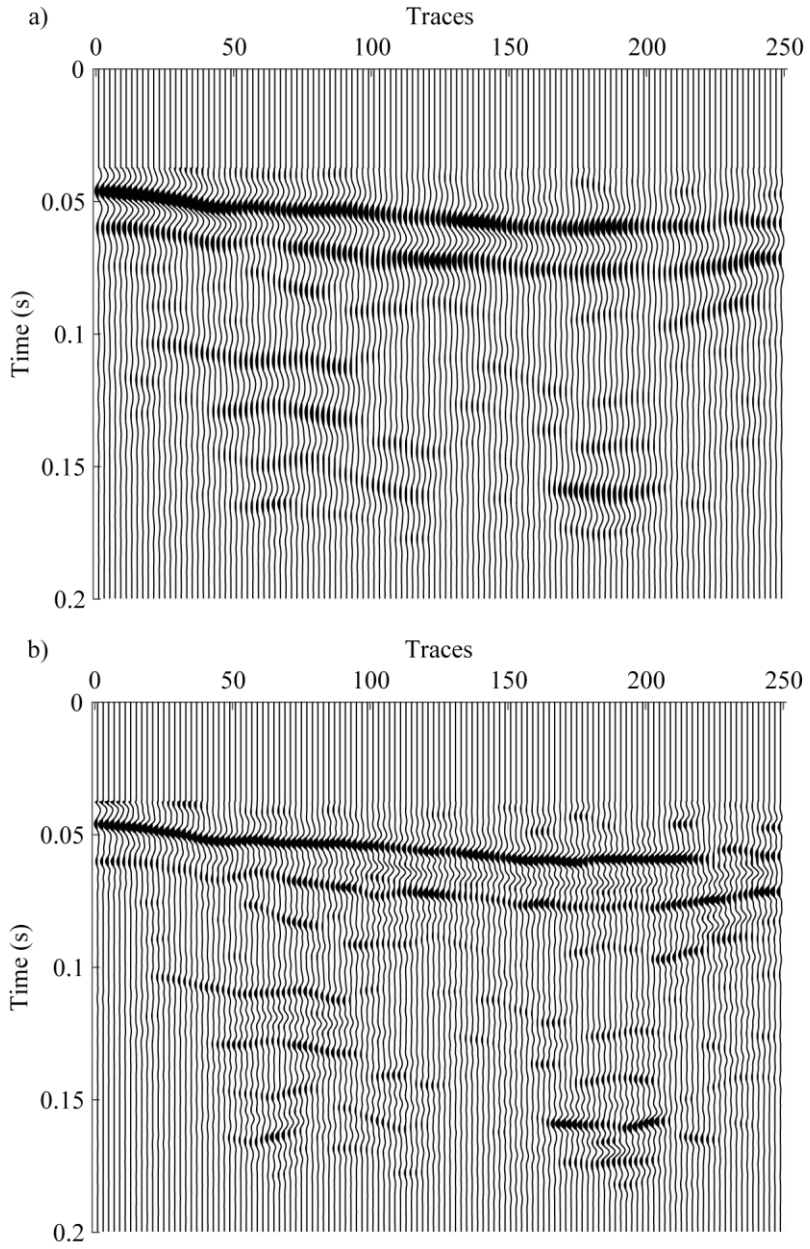

Figure D-7. a) shows the stacked section from Figure 4-6b). b) shows the CNS-ITD results. The estimated reflectivities shown in Figure D-1b) are re-convolved with a stationary 100 Hz Ricker wavelet.

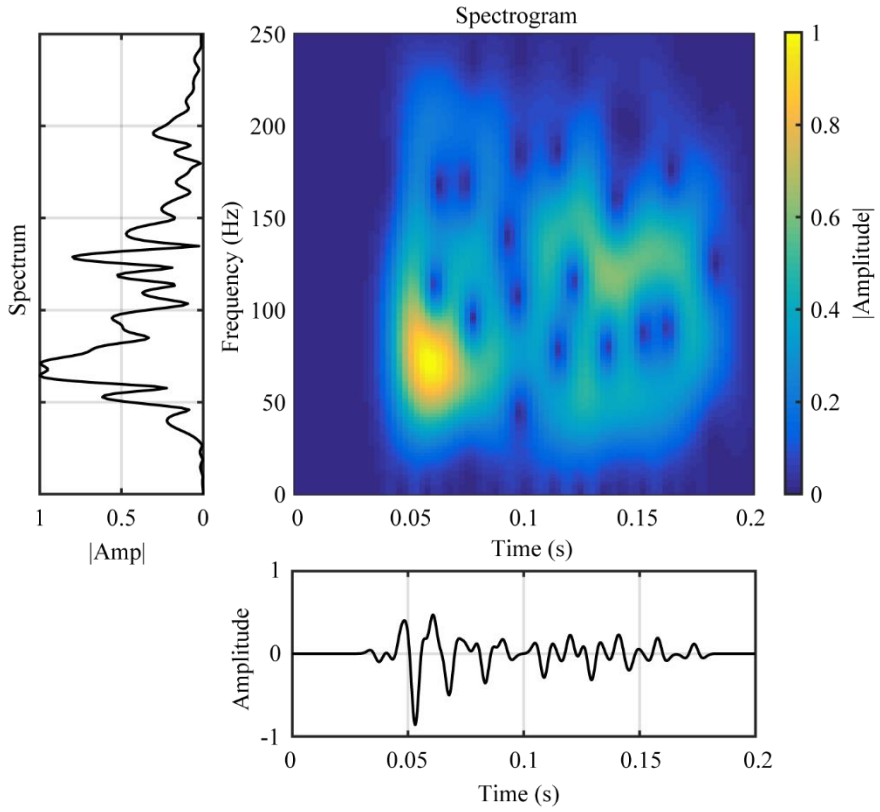

Figure D-8. This figure shows the trace 75 after CNS-ITD application shown in figure D-5b). Note that the estimated reflectivities for trace 75 shown in Figure D-1b) are re-convolved with a stationary 100 Hz Ricker wavelet. The amplitudes on the spectrogram are enhanced for demonstration purposes.

APPENDIX E. COMPARISON OF CNS-ITD WITH WINDOWED STATIONARY ITD

A synthetic example is used to show the differences between continuous non-stationary iterative time-domain deconvolution (CNS-ITD) and windowed stationary ITD, where the propagating seismic wavelet is assumed to be stationary in each window. The non-stationary synthetic trace, which is used in the main text, is divided into several windows and the propagating seismic wavelets are then estimated in each window using the method described in the main text. Figure E-1a shows the non-stationary synthetic trace together with window functions, and the estimated propagating wavelets are shown in E-1b). CNS-ITD is then performed by interpolating the estimated wavelets along the seismic trace which is shown in Figure E-1c) along with the true reflectivity. As can be seen that the reflectivities are all estimated with small amplitude mismatches. Similarly, windowed stationary ITD is also performed using the same estimated propagating wavelets shown in E-1b), assuming they do not change within each sub-window. The result of windowed stationary ITD is also shown in E-1c). As can be seen several reflectivities are under-estimated, and some reflectivities, particularly at later times, are incorrectly located resulting from the broadening effect of the attenuation.

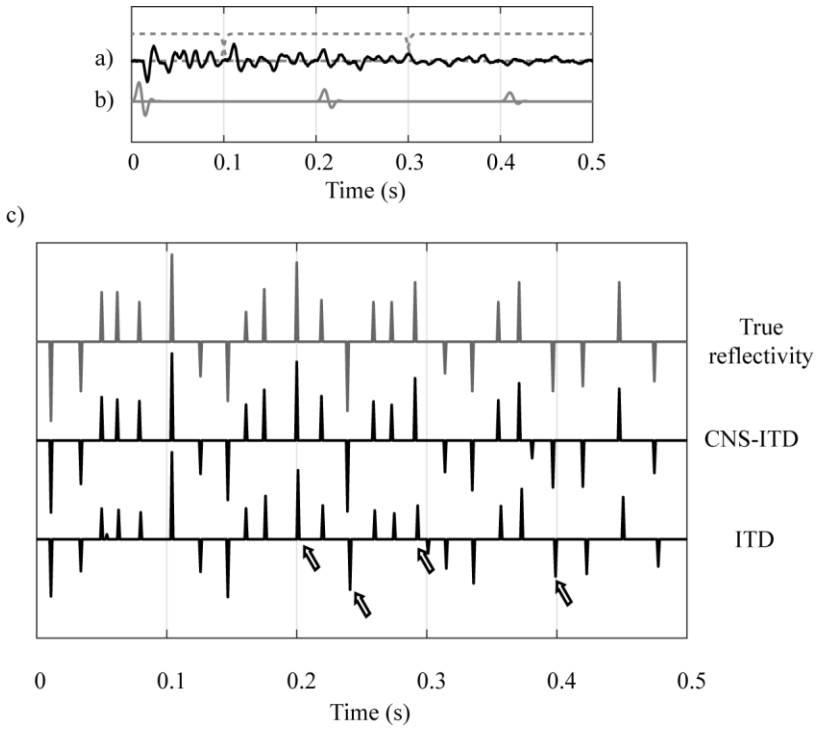

Figure E-1. This figure compares the CNS-ITD approach with the windowed stationary ITD, where the estimated propagating wavelets are assumed to be stationary in each sub-window. a) shows the synthetic non-stationary trace along with the window functions, and b) shows the estimated propagating wavelets in each window. The true reflectivity used in forming synthetic trace, the results of CNS-ITD and windowed stationary ITD are shown in c). As can be seen, the CNS-ITD approach has recovered all the reflectivities with high accuracy. Using the windowed stationary ITD approach, several reflectivities are under-estimated and incorrectly located, which are indicated with the arrows.